Studies of Tracking and Reconstruction in ATLAS: GPU-based Strip Clustering and Optimization of a Run 3 Search for Higgs Decays to Dark Photons

by

Jianan (David) Lai

A thesis accepted and approved in partial fulfillment of the

requirements for the degree of

Master of Science

in Physics

Dissertation Committee:

Stephanie Majewski, Chair

Spencer Chang, Member

David Strom, Member

University of Oregon

Spring 2026

© 2026 Jianan (David) Lai
All rights reserved.

THESIS ABSTRACT

Jianan (David) Lai

Master of Science in Physics

Title: Studies of Tracking and Reconstruction in ATLAS: GPU-based Strip Clustering and Optimization of a Run 3 Search for Higgs Decays to Dark Photons

This thesis presents two independent studies: a GPU-based strip-clustering algorithm designed for the high-luminosity environment of the ATLAS experiment at the Large Hadron Collider (LHC) and an optimization of an ATLAS Run 3 search for Higgs boson decays to dark photons.

The first study focuses on the development and validation of a strip-detector clustering algorithm in `Traccc`, a GPU-accelerated tracking toolkit (usable for both offline track reconstruction and the online trigger system) designed to outperform traditional CPU-based algorithms. To support increased data processing in a higher-collision-rate environment during the Phase-II upgrade program for the High-Luminosity LHC (HL-LHC), we propose Event Filter (EF) Tracking GPU pipelines that employ GPU-based algorithms. The strip clusterization algorithm groups cell hits from silicon strip sensors to form measurements and is integrated into the EF Tracking GPU pipelines in the `ATHENA` framework. The algorithm is validated and shows good consistency in comparing differences in local measurement positions between `TRACCC` and `ATHENA`.

Alongside this detector-focused work, there is a contribution to a search for Higgs boson decays to photons + dark photons produced via gluon-gluon fusion. The search is based on an integrated luminosity of 135 fb^{-1} from ATLAS Run 3 data. Motivated by finding a potential candidate for dark matter, we

search for events with the final state of a Standard Model (SM) photon, missing transverse energy ($E_{\mathrm{T}}^{\mathrm{miss}}$), and collimated sprays of hadrons called jets. My analysis aims to maximize the signal-to-background significance by optimizing selection criteria based on distributions of various variables. A Machine Learning (ML) classifier study, including Boosted Decision Tree (BDT) and Deep Neural Network (DNN) approaches, was also developed to further enhance signal sensitivity. After optimizing the selection criteria, the analysis improved the expected upper limit on the branching ratio of this process by 70% (from 1.3 to 0.75) compared to the previous work.

This thesis includes previously published co-authored material.

CURRICULUM VITAE

NAME OF AUTHOR: Jianan (David) Lai

GRADUATE AND UNDERGRADUATE SCHOOLS ATTENDED:

University of Oregon, Eugene, OR, USA
University of Washington, Seattle, WA, USA

DEGREES AWARDED:

Master of Science, Physics, 2026, University of Oregon
Bachelor of Science, Physics, 2024, University of Washington

AREAS OF SPECIAL INTEREST:

PROFESSIONAL EXPERIENCE:

GRANTS, AWARDS AND HONORS:

PUBLICATIONS:

ATLAS Collaboration, "*Search for dark photons from Higgs boson decays in the gluon-gluon fusion channel in proton-proton collisions at* $\sqrt{s} = 13.6$ *TeV with the ATLAS detector*", submitted to JHEP.

ACKNOWLEDGEMENTS

I would like to express my sincere gratitude to my advisor, Stephanie Majewski, for her continuous support and guidance throughout my Master's studies at the University of Oregon. I am also deeply grateful to the committee members, Spencer Chang and David Strom, for their feedback and time spent reviewing my work and in my Master's Thesis defense.

I gratefully acknowledge all the assistance I received from Federica Piazza, Timothy Mathew, and the dark photon group in conducting the dark photon study. I also want to thank Fabrice Le Goff, Neza Ribaric, and Benjamin Michael Wynne for their technical assistance and invaluable insights for my strip clustering research. Finally, I want to thank my family and friends for their financial and emotional support in completing my Master's degree.

TABLE OF CONTENTS

Chapter Page

I. INTRODUCTION 17

1.1. The Standard Model of particle physics 17

1.1.1. Brief Overview of SM particles and interactions 17

1.1.2. Role of the Higgs boson 21

1.2. Beyond the Standard Model 24

1.3. Large Hadron Collider (LHC) and A Toroidal LHC Apparatus (ATLAS) 27

1.3.1. Introduction 27

1.3.1.1. Luminosity 28

1.3.1.2. Pile-up 30

1.3.2. Timeline of LHC and ATLAS Data-Taking Runs 32

1.3.2.1. Run 1 (2010–2012) 32

1.3.2.2. Run 2 (2015–2018) 32

1.3.2.3. Run 3 (2022–2026) 33

1.3.2.4. Long Shutdown 3 and Run 4 (HL-LHC Era) 33

1.3.3. The ATLAS Detector 34

1.3.4. Trigger and Data Acquisition System 36

1.4. ATLAS Run 4 Upgrade 36

II. ATLAS EVENT FILTER (EF) TRACKING: STRIP CLUSTERING 40

2.1. Introduction 40

2.1.1. Overview of GPU-based pipelines 41

2.1.1.1. Inner Tracker (ITK) Strip Detectors 43

Chapter Page

2.1.1.2. Motivation for GPU Implementation 45
2.1.2. Strip clustering algorithm 45
2.1.3. Integration with the `Traccc` framework 50
2.2. Results and Discussion 50
2.2.1. Cluster comparison with CPU 50
2.2.2. Summary of EF Tracking validation 54
III. ATLAS: SIGNAL OPTIMIZATION OF A SEARCH FOR HIGGS DECAYS TO DARK PHOTONS USING ATLAS RUN 3 DATA 55
3.1. Title 55
3.2. Disclaimer 55
3.3. Abstract 55
3.4. Introduction 56
3.4.1. Motivation for Hidden Sectors 56
3.4.2. Dark Photon 56
3.5. Data and MC samples 58
3.5.1. Data samples 58
3.5.2. MC samples 59
3.6. Physics object reconstruction and identification 60
3.7. Event selection 64
3.7.1. Trigger 64
3.8. Signal region optimization 64
3.8.1. N-1 iteration method 65
3.8.2. Statistical method 67
3.8.3. Machine Learning approach 76

Chapter Page

3.8.3.1. Boosted Decision Tree (BDT) training and results 76

3.8.3.2. TRExFitter for BDT 81

3.8.3.3. Neural Network (NN) training and results 83

3.9. Conclusions and Outlook 89

APPENDIX: DARK PHOTON: DATA AND MC SAMPLES 91

REFERENCES CITED 97

LIST OF FIGURES

Figure Page

1. Elementary particles of the Standard Model [1]. 18

2. The two possible neutrino mass hierarchies, normal where $m_3 > m_2$ and inverted where $m_2 > m_3$ [2]. 21

3. Feynman diagrams contributing to the Higgs production in (a) Gluon-Gluon fusion, (b) Vector Boson Fusion, (c) Higgsstrahlung, and (d) Top Associated Production [3]. 24

4. Leading-order contributions to the decay of the Higgs boson into two photons [4]. 25

5. Schematic of CERN accelerator complex how the protons are produced and accelerated to four interaction points [5]. 29

6. Cut view of the ATLAS Detector in Run 3 [6]. 30

8. Vertex topologies in ATLAS, including primary (red), secondary (blue), and pile-up (red) vertices [7]. 31

9. ATLAS detector slice with labeled subdetectors and particle visualizations [8] 35

10. ATLAS Trigger and Data Acquisition System in Run 4 [9] 39

11. Overview of the reconstruction pipelines, including the G-050, G-130, and G-200 pipelines discussed in this thesis. 43

12. Stave with 14 Short Strip modules. The sensor consists of two hybrids and one power board [10]. 44

13. A view of the end-cap petal with six silicon modules and an EoS card placed on each side [11]. 44

14. The layout of the ATLAS ITK, where the red represents the pixel detectors, and the blue represents the strip detectors (horizontal blue lines are barrel, and vertical are annulus) [12]. 46

Figure Page

16. Residue of Local Position (x, y) between TRACCC and ATHENA (CPU) outcome, where top and bottom plots are annulus, and the middle plots are barrel modules. The accuracy is within $\mathcal{O}(10^{-10})$ mm. 51

17. Validation of strip cluster local coordinates and η dependence. 52

18. Global coordinate distributions for the strip clusters. 53

19. Feynman diagram illustrating the Higgs boson production via gluon-gluon fusion process (top) and vector-boson fusion (VBF) and Higgsstrahlung (VH) processes (bottom left and right), all followed by the decay into a photon and a dark photon ($H \rightarrow \gamma\gamma_d$). The hatched circle in the $H\gamma\gamma_d$ vertex represents the interaction through messenger fields. 57

20. Iteration workflow for optimizing the cut set using n-1 studies and significance checks. 65

21. Pre-fit (left) and post-fit (right) distributions for the Signal Region (SR) and the 1μ Control Region (CR). 69

22. Pre-fit (left) and post-fit (right) distributions for the 2μ Control Region (CR) and the Low MET Significance Control Region (CR). Generated by Tim Matthew (senior PhD at the University of Oregon). The m_T distributions span 80–300 GeV with binning (80, 110, 140, 200, 300) GeV. 70

23. Normalization factors k_{W_γ} and k_{Z_γ} and branching ratio BR($H \rightarrow \gamma\gamma_d$) with their corresponding statistical uncertainties (+data-driven systematics only, no experimental or theoretical systematics) for optimized selection fitter. 71

24. Observed and expected 95% CL upper limits on the branching ratio $\mathcal{B}(H \rightarrow \gamma\gamma_D)$ obtained from the individual analysis channels and their combination. The black markers indicate the observed limits, while the dashed line represents the median expected limit under the background-only hypothesis. The green and yellow bands correspond to the $\pm1\sigma$ and $\pm2\sigma$ intervals on the expected limit, respectively [13]. . . . 71

25. Additional Selection variables distributions after the optimized rectangular cuts for the ggF $H \rightarrow \gamma\gamma_D$ analysis. 74

Figure Page

26. N−1 distributions for the ggF $H \to \gamma\gamma_D$ analysis. 75

27. Correlation matrix of the BDT input variables after the baseline selection. The absolute value of the correlation above 0.75 will drop one of the two variables based on their physical significance and their AUC of ROC. 77

28. Weight and Biases plot [14] for the 95 BDT Sweeps (null runs were excluded), where it records the hyperparameters (gamma, learning rate, max depth, number of estimators, subsample) and performance (test AUC of the ROC, best $\frac{S}{\sqrt{B}}$, its corresponding ML BDT Score cut and acceptance rate). The highlighted line is the chosen parameter in table 11. 79

29. Significance versus BDT score threshold, with the maximum simple significance at BDT score $\geq$ 0.02. $S/\sqrt{B}$ (blue) is the simple counting significance; $S/\sqrt{S+B}$ is (orange) the poisson-aware approximation; $S/\sqrt{S+1.3B}$ (green) is the Ad-hoc systematic-aware metric, assuming 30% background systematic; Zbi (red) is the Binomial significance. 80

30. Receiver Operating Characteristic (ROC) curve (Left) and feature importance of input variables for the trained Boosted Decision Tree (BDT) model 81

31. TRExFitter result for Boosted Decision Tree (BDT). m_T distributions before and after the pre-selections and ML BDT score cut for Signal Region (SR). The 1μ Control Region (CR), the 2μ CR, and the Low Met significance CR are the same as 22 82

32. Normalization factors k_{W_γ} and k_{Z_γ} and branching ratio BR($H \to \gamma\gamma_d$) with their corresponding statistical uncertainties (+data-driven systematics only, no experimental or theoretical systematics) for ML BDT score cut TRExFitter. 82

33. Significance versus NN score threshold. The maximum simple significance ($S/\sqrt{B} = 2.915$) is achieved at NN score $\geq$ 0.91, corresponding to a signal acceptance of 58%. 86

Figure Page

34. TRExFitter result for Deep Neural Network (DNN). m_T distributions before and after the pre-selections and ML BDT score cut for Signal Region (SR). The 1μ Control Region (CR), the 2μ CR, and the Low Met significance CR are the same as 22 87

35. Weight and Biases plot [14] for the 50 DNN Sweeps, where it records the hyperparameters (gamma, learning rate, max depth, number of estimators, subsample) and performance (test AUC of the ROC, best $\frac{S}{\sqrt{B}}$, its corresponding ML BDT Score cut and acceptance rate). The highlighted line is the chosen parameter in table 11. 88

LIST OF TABLES

Table Page

1. Average timing of the different steps of track reconstruction using the G-080 pipeline for $t\bar{t}$ events at $\langle\mu\rangle = 140$ and $\langle\mu\rangle = 200$. Since both pixel and strip clustering were sent to the GPU, the clustering timing includes both. HS23 refers to HEPScore23, a CPU performance benchmark used to evaluate and quantify computing power. 52
2. Summary of the Good Run Lists (GRL) and integrated luminosities used for the Run 3 analysis. 58
3. Electron selection criteria. 61
4. Jet reconstruction criteria. 61
5. Muon selection criteria. 62
6. Overlap removal criteria. 62
7. Photon selection criteria. 63
8. Preselections and basic-cut comparison between the Internal Note and Optimized Selections 66
9. Final event selections. The SR uses the optimized cuts, while the control regions use the nominal cuts. 72
10. A table with optimized cuts on the signal region and retaining the nominal cuts on the control region for the input to TRExFitter. 72
11. Hyperparameter distribution in the randomized BDT sweep and the parameters for the best run 78
12. Model of the Deep Neural Network (DNN) Classifier 84
13. Hyperparameter search ranges used in the neural network Bayesian sweep and the best-performing configuration. 84
14. Comparison of the four methods with their performance in observed and expected limit, significance, and significance $\times$ acceptance. . 89

Table Page

A.15List of signal MCd samples used in this analysis. 91

A.16List of W/Z MC23d and MC23e samples used in this analysis. 91

A.17List of $\gamma jets$ MC23d and MC23e samples used in this analysis. 94

A.18List of $W\gamma/Z\gamma$ MC23d and MC23e samples used in this analysis 95

A.19Pre-fit Weighted Event Yields after Nominal Cuts for each process and data. 95

A.20Pre-fit Weighted Event Yields after Optimized Cuts for each process and data. 96

CHAPTER I

INTRODUCTION

1.1 The Standard Model of particle physics

1.1.1 Brief Overview of SM particles and interactions.

The Standard Model of particle physics is a relativistic quantum field theory that describes the elementary particles known to date that constitute matter and the four fundamental forces of nature (except gravity). At the Large Hadron Collider (LHC), the most recent particle discovery was the Higgs boson in 2012, which is responsible for electroweak symmetry breaking and mass generation [15].

This chapter introduces the components of the Standard Model and their significance, while the next section, beyond the Standard Model, explains its limitations.

Elementary particles in the Standard Model are described by a quantum field theory, corresponding to the symmetry group

$$SU(3)_C \times SU(2)_L \times U(1)_Y.$$

There are two classes of particles in the Standard Model, which are fermions or bosons. Each particle has its own antiparticles: charged particles have antiparticles with opposite charge, while all other properties remain the same [16] [2].

Fermions are the matter particles that have spin $\frac{1}{2}$. In the Standard Model, there are six different fermion flavors (three quark flavors and three lepton flavors), split into three generations, all of which follow Fermi-Dirac statistics. The Pauli Exclusion Principle, which is a direct result of the Fermi-Dirac statistics, states that no two fermions can occupy the same quantum state. This is why an electron

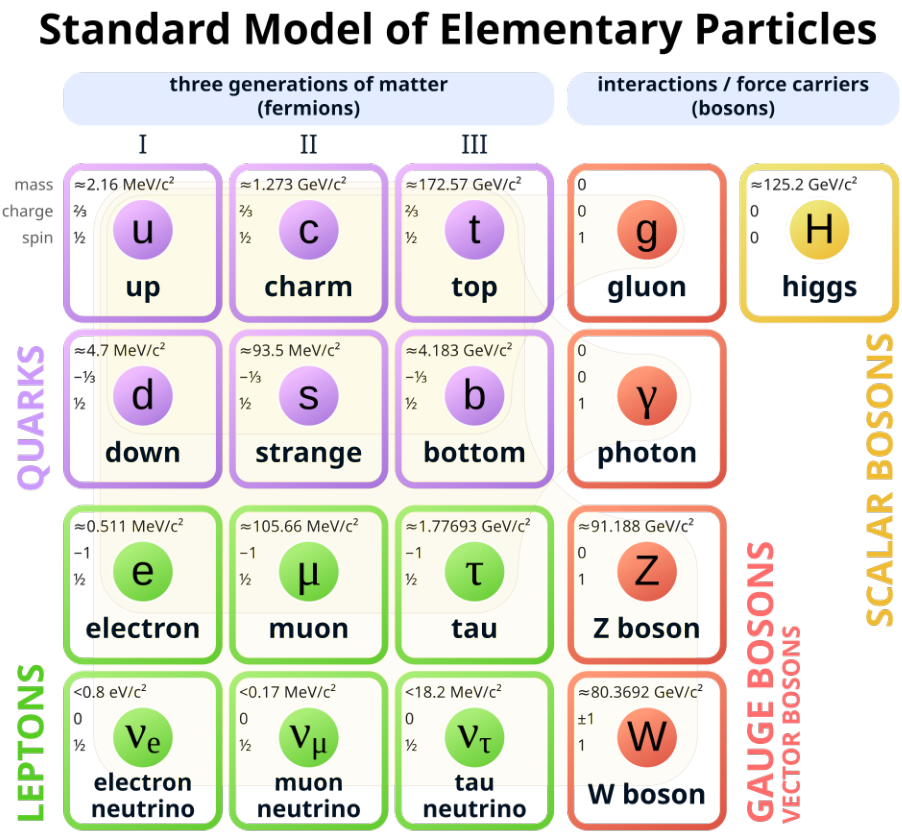


Figure 1. Elementary particles of the Standard Model [1].

will move up to a higher energy state in an atom if all of the lower energy states are already occupied by other electrons.

The six flavors of quarks are up, down, charm, strange, top, and bottom quarks. Organized by generations, the increasing mass from left to right, the quarks are represented as:

$$\begin{pmatrix} u \\ d \end{pmatrix}, \begin{pmatrix} c \\ s \end{pmatrix}, \begin{pmatrix} t \\ b \end{pmatrix}$$

The first row of the quarks possesses a fractional charge of $+\frac{2}{3}$; the second row has $-\frac{1}{3}$. Their corresponding antiparticles are

$$\begin{pmatrix} \bar{u} \\ \bar{d} \end{pmatrix}, \begin{pmatrix} \bar{c} \\ \bar{s} \end{pmatrix}, \begin{pmatrix} \bar{t} \\ \bar{b} \end{pmatrix}$$

All these quarks have a non-Abelian charge called color charge from the local gauge symmetry $SU(3)_c$ of quantum chromodynamics (QCD). Because of color confinement, the quarks do not appear as free particles but as color-neutral bound states, called hadrons. There are two classes of hadrons: the mesons, consisting of a quark and an antiquark, and the baryons, consisting of three quarks or three antiquarks. Mesons are color neutral because the color of a quark is canceled by the anticolor of the corresponding antiquark, such as the triplets of pions (π^+, π^0, π^-). The three quarks that make up the baryons have colors, red, green, and blue, which are balanced to give a color-neutral object. The two well-known baryons are the proton (p) and the neutron (n). Quarks interact through all four fundamental forces. The strong force, mediated by gluons, binds quarks into hadrons; the electromagnetic and weak interactions are responsible for charge and flavor changes; the gravitational force, due to its small magnitude, is irrelevant compared to the other three forces.

The leptons are the electron, muon, tau, electron neutrino, muon neutrino, and tau neutrino. Organized by generations and increasing mass from left to right, the leptons are:

$$\begin{pmatrix} e^- \\ \nu_e \end{pmatrix}, \begin{pmatrix} \mu^- \\ \nu_\mu \end{pmatrix}, \begin{pmatrix} \tau^- \\ \nu_\tau \end{pmatrix}.$$

The first row of leptons has a charge of -1, and neutrinos are charge-neutral and left-handed. Their corresponding anti-particles are

$$\begin{pmatrix} e^+ \\ \bar{\nu_e} \end{pmatrix}, \begin{pmatrix} \mu^+ \\ \bar{\nu_\mu} \end{pmatrix}, \begin{pmatrix} \tau^+ \\ \bar{\nu_\tau} \end{pmatrix}.$$

The first row of anti-leptons becomes +1 charge, and anti-neutrinos are right-handed.

Charged leptons interact via the electromagnetic, weak, and gravitational interactions, whereas neutrinos interact only via the weak and gravitational interactions, making them weakly interacting and difficult to detect. The theory predicts that the neutrinos are massless. However, neutrino oscillations are the most direct evidence that neutrinos have nonzero masses, although these masses are very small. We have yet to determine the individual neutrinos' masses, only their upper limits.

$$\sum_{i=1}^{3} m_{\nu_i} \leq 1\,\mathrm{eV} \tag{1.1}$$

Neutrino oscillation experiments only determine the squared mass differences among the three neutrino mass eigenstates, which yield [17]

$$\begin{aligned} \Delta m^2_{21} = m_2^2 - m_1^2 = (7.60 \pm 0.17) \times 10^{-5}\,\mathrm{eV}^2 \\ |\Delta m^2_{32}| = |m_3^2 - m_2^2| = (2.52 \pm 0.04) \times 10^{-3}\,\mathrm{eV}^2 \end{aligned} \tag{1.2}$$

Based on this information, we don't know the exact hierarchy of neutrino masses; there are two possible hierarchies: normal ($m_3 > m_2$) and inverted ($m_2 > m_3$), as shown in Fig. 2.

The Bosons are four Spin-1 gauge Bosons plus one Spin-0 Higgs Boson. The four spin-1 gauge Bosons are the mediators of the four fundamental forces of nature. The massless photon is the mediator of the electromagnetic force. The $W^\pm$

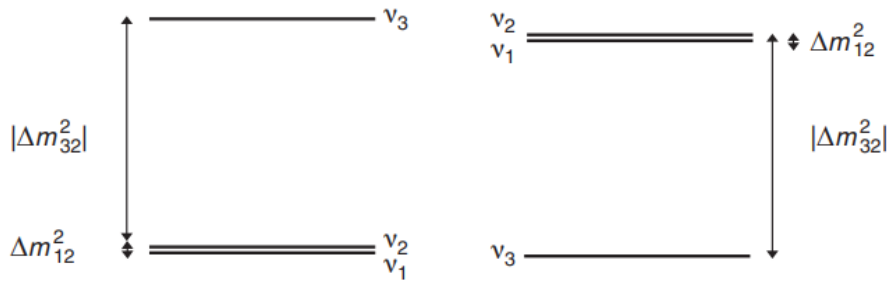


Figure 2. The two possible neutrino mass hierarchies, normal where $m_3 > m_2$ and inverted where $m_2 > m_3$ [2].

and Z Bosons are the mediators of the weak force. The eight color-carrying gluons are the mediators of the strong force between the quarks. There is no gauge Boson in the Standard Model for the gravitational force. In addition to gauge bosons, the Standard Model contains the Higgs boson, a scalar (spin-0) particle associated with the Higgs field, whose nonzero vacuum expectation value gives rise to the masses of elementary fermions and weak gauge bosons through spontaneous electroweak symmetry breaking.

—

1.1.2 Role of the Higgs boson. The electroweak theory unifies the electromagnetic and weak interactions; it predicts that the gauge bosons, fermions, and neutrinos are massless, whereas the experimental results suggest otherwise [2]. In 1964, Brout, Englert, and Higgs proposed the Higgs mechanism that explains the origin of mass for those particles while preserving gauge invariance. The Higgs mechanism introduces a SU(2) doublet of a spin-0 complex field, namely the Higgs field, transforming under the electroweak gauge group $SU(2)_L \times U(1)_Y$,

$$\Phi = \begin{pmatrix} \phi^+ \\ \phi^0 \end{pmatrix}, \tag{1.3}$$

where the ϕ^0 and ϕ^+ are the neutral and charged components of the Higgs field accordingly.

The Lagrangian for the Higgs field is

$$\mathcal{L} = (\partial_\mu \Phi)^\dagger (\partial^\mu \Phi) - V(\Phi), \tag{1.4}$$

where the Higgs potential is

$$V(\Phi) = \mu^2 \Phi^\dagger \Phi + \lambda (\Phi^\dagger \Phi)^2. \tag{1.5}$$

For $\mu^2 < 0$ and $\lambda > 0$, the potential has infinite number of minima at $|\Phi| = \frac{v}{\sqrt{2}} = \sqrt{\frac{-\mu^2}{2\lambda}}$. To ensure the photon remains massless, the vacuum state must be electrically neutral so that the electromagnetic symmetry is preserved. Therefore, the vacuum expectation value (VEV) of the Higgs field is

$$\langle \Phi \rangle = \frac{1}{\sqrt{2}} \begin{pmatrix} 0 \\ v \end{pmatrix}, \tag{1.6}$$

where $v = \sqrt{-\mu^2/\lambda} \approx 246$ GeV is determined experimentally. The $SU(2)_L \times U(1)_Y$ electroweak gauge symmetry is spontaneously broken down to the $U(1)_{EM}$ symmetry. One can choose the unitary gauge and write the Higgs doublet as

$$\langle \Phi \rangle = \frac{1}{\sqrt{2}} \begin{pmatrix} 0 \\ v + h(x) \end{pmatrix}, \tag{1.7}$$

which the h(x) corresponds to the fluctuation of the vacuum state. Three of the four degrees of freedom defer to the longitudinal components of $W^\pm$ and Z bosons, while the remaining degree of freedom h(x) is the physical Higgs boson. Their masses are

$$m_{W^\pm} = \frac{1}{2} g v, \qquad m_Z = \frac{1}{2} \sqrt{g^2 + g'^2}\, v, \qquad m_H = \sqrt{2\lambda}\, v, \tag{1.8}$$

with experimentally measured values of $m_{W^\pm} = 80.3625 \pm 0.0077$ GeV, $m_Z = 91.1979 \pm 0.0020$ GeV, and $m_H = 125.20 \pm 0.11$ GeV as reported by the Particle Data Group [17].

Moreover, fermions gain their mass through Yukawa interactions in the Higgs mechanism. The Lagrangian is written as

$$\mathcal{L}_{\text{Yukawa}} = -y_f \bar{\psi}_L \Phi \psi_R + \text{h.c.}, \tag{1.9}$$

where ψ_L and ψ_R are the left-handed and right-handed fermion fields, respectively; "h.c." denotes the Hermitian conjugate, leading to fermion mass

$$m_f = \frac{y_f v}{\sqrt{2}}, \tag{1.10}$$

where y_f denotes the Yukawa coupling of fermion f. From the equation, fermion masses are directly related to the Yukawa coupling strength with the Higgs field. For instance, the top quark has the largest mass in the Standard Model with $m_t \approx 172.5$ GeV, and its Yukawa coupling, $y_t \approx 1$. In comparison, an electron has a mass of $m_e \approx 0.5$ MeV and Yukawa couplings of $y_e \approx 2.9 \times 10^{-6}$.

At the LHC, there are four primary ways to produce Higgs bosons: gluon-gluon fusion ($gg \to H$), mediated by a top-quark loop, which accounts for $\sim 88\%$ of the total Higgs production cross section, Vector Boson Fusion (VBF) at $\sim 7\%$, Higgsstrahlung (VH) at $\sim 4\%$, and Top Associated Production ($t\bar{t}H$) at $\sim 1\%$ [17]. The corresponding Feynman diagrams are shown in Fig. 3. Since gluons carry approximately 48% of protons' total momentum, gluon interaction dominates over quarks when protons collide at nearly the speed of light.

After being produced, the Higgs boson decays into several Standard Model final states. The dominant decay channel is $H \to b\bar{b}$ at $53 \pm 8\%$ of total decay yield, while other decay modes are $H \to WW^*$, $H \to ZZ^*$, $H \to \tau^+\tau^-$, and $H \to \gamma\gamma$

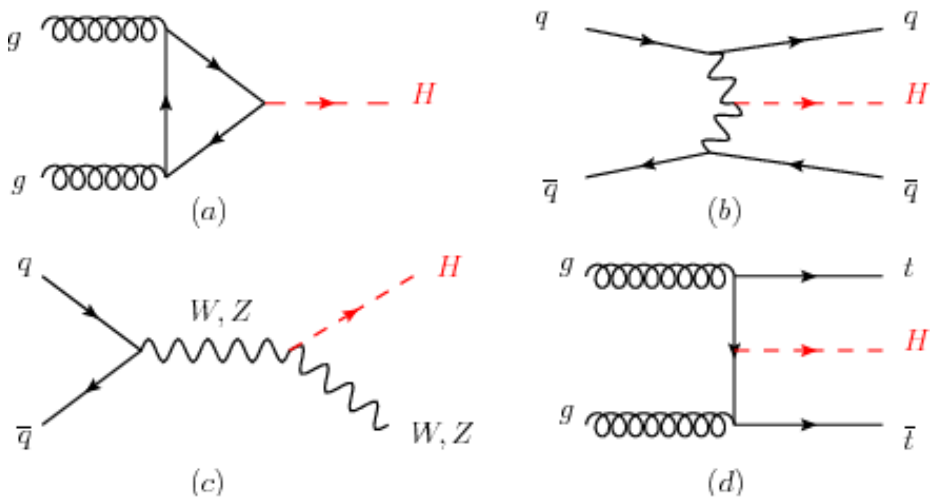


Figure 3. Feynman diagrams contributing to the Higgs production in (a) Gluon-Gluon fusion, (b) Vector Boson Fusion, (c) Higgsstrahlung, and (d) Top Associated Production [3].

mediated by a W-boson or top-quark loop [17]. The Feynman diagrams for the diphoton decay channel are shown in Fig. 4.

Unlike the gauge bosons, the Higgs boson is not a force mediator but plays the most important role of setting the mass scale of the Standard Model. Due to its unique properties, the Higgs boson provides a sensitive gateway to potential beyond-the-Standard-Model physics.

—

1.2 Beyond the Standard Model

The Standard Model provides a successful description of the known elementary particles and their interactions. Various experimental measurements confirm the model's predictions. However, the model has limitations that cannot explain some experimental observations, prompting researchers to search for Beyond the Standard Model (BSM) physics [17] [2].

As briefly mentioned in Subsection 1.1.1, electromagnetic, weak, and strong interactions, with their corresponding mediator particles, are incorporated into

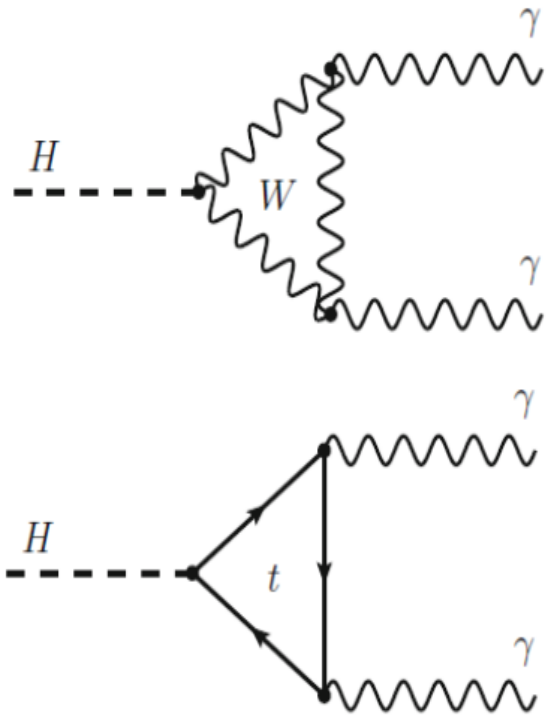


Figure 4. Leading-order contributions to the decay of the Higgs boson into two photons [4].

the quantum field theoretical framework, whereas gravity is currently understood only through classical mechanics and general relativity. The theory posits a force carrier for gravity, gravition (a massless, neutral-charged, spin-2 boson), which has not been experimentally observed. Mathematically, the theory of quantum gravity treats the force carrier as a point particle, leading to an infinite, non-renormalizable result when calculating the graviton-graviton interaction.

The Standard Model also fails to account for the existence of dark matter, which makes up around 26.8% of the whole universe [18]. Astrophysical and cosmological observations, including galaxy rotation curves [19], gravitational lensing [20], and measurements of the cosmic microwave background [18], provide

compelling evidence for a non-luminous form of matter that constitutes a significant fraction of the universe's energy density. However, none of the Standard Model particles satisfy the properties of dark matter. For instance, in the later Section III, we propose the potential existence of a dark photon where the Standard Model Higgs boson can decay to a SM photon and a massless dark photon via a hypothetical mediator field.

There is also the flavor problem that remains unexplained, concerning the three generations, the mass hierarchy, and the mixing angles. The Standard Model organized the particles into three generations, yet there is no fundamental justification for this. Secondly, the masses of the particles are determined by the Yukawa coupling constants to the Higgs field, which are experimentally determined. The mass of the electron is approximately $0.511\,\mathrm{MeV/c^2}$, whereas the top quark mass is about $(172.56 \pm 0.32)\,\mathrm{GeV/c^2}$ [17]. Such a drastic mass difference means there is no symmetry or principle to predict their coupling strength. Moreover, particles can transit from one flavor to another. Quark mixing is governed by the Cabibbo-Kobayashi-Maskawa (CKM) matrix, which connects their weak and mass eigenstates. Within this framework, the mixing angles are relatively small, indicating the quarks' tendency to stay within their generations. Nevertheless, neutrino mixing is described by the Pontecorvo–Maki–Nakagawa–Sakata (PMNS) matrix, in which the mixing angles are relatively large. As a result, the neutrinos are in flavor states that are a superposition of the mass states (ν_1, ν_2, ν_3). The difference in mass causes a discrepancy in travel speed and phases, forming a new combination that resembles a muon neutrino rather than an electron neutrino, for example. This is the neutrino oscillation.

Another unresolved issue is the neutrino masses. The Standard Model predicts that the neutrinos are exactly massless due to the absence of right-handed neutrino fields and Yukawa couplings. Nonetheless, experimental observations of neutrino oscillations demonstrate nonzero masses and flavor-state interconversions [21] [22]. Explaining these masses requires introducing new particles, new interactions, or higher-dimensional operators beyond the Standard Model.

In addition, the Standard Model does not explain the observed matter–antimatter asymmetry of the universe [23]. Although it contains sources of CP violation in the quark sector, these effects are insufficient to account for the baryon asymmetry generated in the early universe. Additional sources of CP violation or departures from thermal equilibrium are therefore required.

All in all, these open questions encourage searches for physics beyond the Standard Model both theoretically and experimentally.

—

1.3 Large Hadron Collider (LHC) and A Toroidal LHC Apparatus (ATLAS)

1.3.1 Introduction. The Large Hadron Collider, or LHC for short, is a huge circular tunnel that stretches for 26.7 kilometers underground near the Swiss-French border. Inside this tunnel, protons are accelerated to nearly the speed of light and then made to collide with each other every 25 ns (40 MHz) at four interaction points: ATLAS (Interaction Point 1), CMS, LHCb, and ALICE. For this thesis, I am focusing on research in ATLAS.

As shown in Fig. 5, the process starts with a bottle of hydrogen gas, which is used to create H^- ions with an electric field. Linac 4, commissioned to replace

the older Linac 2, is a linear accelerator to bring the H^- ions to an energy of 160 MeV. Then a carbon foil strips both electrons from the H^- ions, leaving bare protons (p^+).

The protons are then injected into the Proton Synchrontron Booster (PSB), Proton Synchrontron (PS), and Super Proton Synchrontron (SPS), increasing protons' energy to 2.0 GeV, 26 GeV, 450 GeV respectively. Once the protons are accelerated to the required speed, they are sent to the LHC via two transfer lines (TI 2 and TI 8) and collide at the four interaction points.

A Toroidal LHC ApparatuS (ATLAS) is a general-purpose particle physics experiment at Interaction Point 1 (IP1) of the LHC [24]. As shown in Fig. 6, the cut view of ATLAS shows that the detectors cover almost all angular directions for proton collisions at the interaction point. Its purpose is to capture all particle information produced by the collision in each layer of the detector, tailored to each particle's properties. Then, with the collected positions and deposited energy and momentum from all detectors, algorithms can identify the particle and reconstruct its track and collision vertex. For the coordinate system, the z-axis aligns with the beam axis, the x-axis points towards the center of the LHC ring, and the y-axis points upwards. Cylindrical coordinates (r, ϕ) are used in the transverse plane, ϕ being the azimuthal angle around the z-axis. Pseudorapidity is defined in terms of the polar angle θ as $\eta = -\ln\tan(\theta/2)$, which is Lorentz-invariant under boosts along the beamline.

—

1.3.1.1 Luminosity. The physics reach of the ATLAS experiment is limited by the LHC-delivered luminosity. The LHC delivered luminosity, which sets the rate of proton–proton collisions, translates into the number of expected

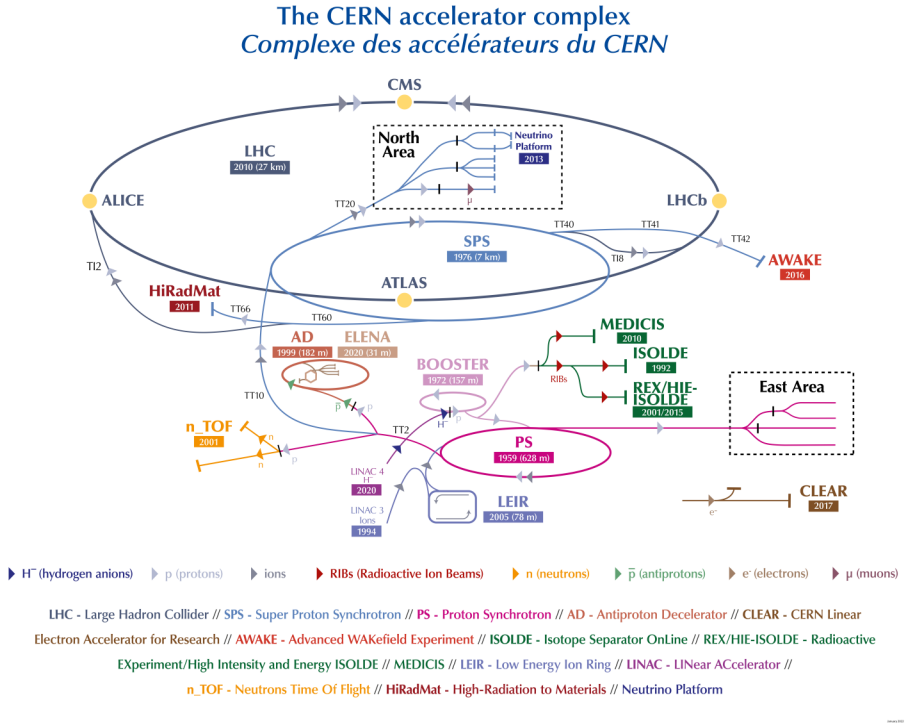


Figure 5. Schematic of CERN accelerator complex how the protons are produced and accelerated to four interaction points [5].

events for a given process and its production cross section. The instantaneous luminosity, $\mathcal{L}$, can be determined from the number of observed events, N, and the corresponding production cross section, σ, by the following equation:

$$N = \sigma \int \mathcal{L}(t)\, \mathrm{d}t. \tag{1.11}$$

The data collected by ATLAS is characterized by the integrated luminosity, L, expressed in inverse femtobarns (fb^{-1}), which gives the total amount of data used for a particular analysis. Fig. 7a shows the integrated luminosity in Run 3 recorded by ATLAS at 322 fb^{-1}, and Fig. 7b illustrates the combined Run 1, 2, 3 integrated luminosity recorded by ATLAS at 505 fb^{-1}.

Higher luminosity means more collision events, enabling more precise measurements of particle mass and coupling strength. However, the increased

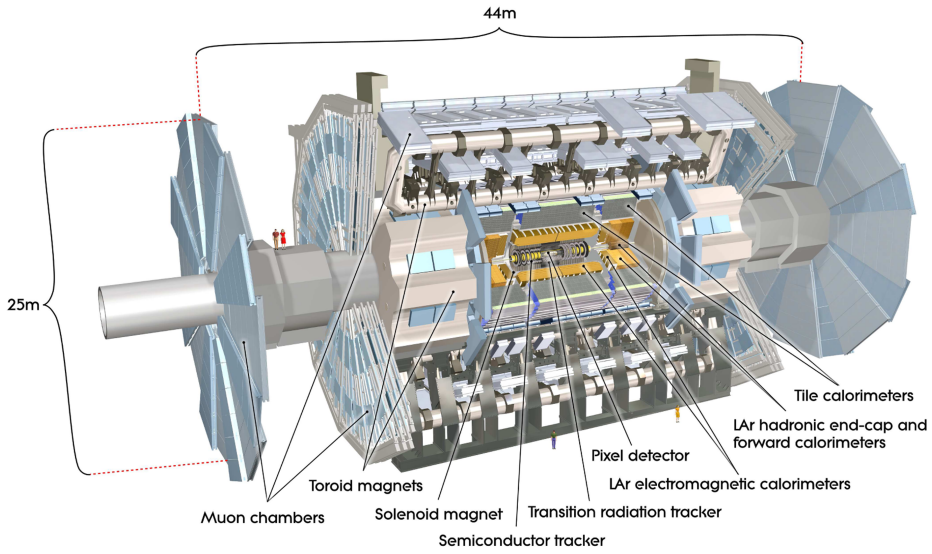
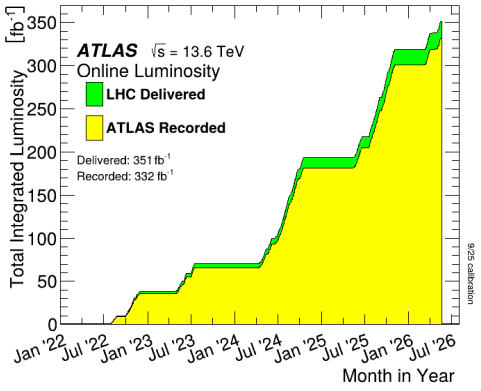
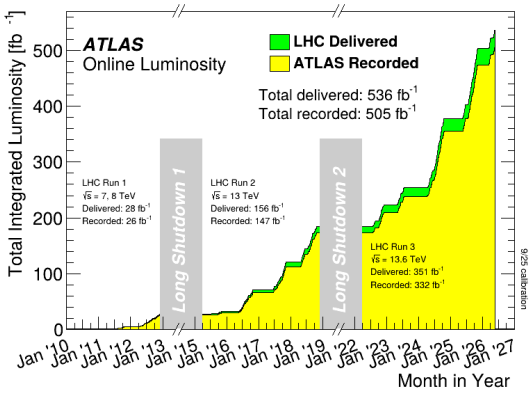


Figure 6. Cut view of the ATLAS Detector in Run 3 [6].

number of particles hitting the detectors means that signals are buried in a large background of other particles, making track reconstruction more difficult.



(a) Cumulative integrated luminosity recorded by ATLAS in LHC Run 3 [25]



(b) Cumulative integrated luminosity recorded by ATLAS in LHC Run 1, 2, 3 combined [25]

1.3.1.2 Pile-up. Pile-up refers to multiple proton-proton interactions occurring within a single bunch crossing. It is commonly quantified by the parameter μ, which represents the average number of inelastic interactions per

bunch crossing. Higher luminosity operation of the LHC directly leads to increased pile-up.

Pile-up interactions contribute additional charged particles and energy deposits that are unrelated to the primary hard-scatter process and to the secondary vertex from b-quark decays, as shown in Fig. 8. These additional interactions can affect track reconstruction, vertex identification, jet energy measurements, and missing transverse momentum reconstruction. As a result, pile-up represents a major experimental challenge, particularly in later LHC runs where luminosity is substantially higher.

To mitigate the effects of pile-up, ATLAS uses a combination of detector design and specialized techniques to reconstruct what happened. This includes precise vertex reconstruction and pile-up-aware object definitions. It's also crucial to accurately model pile-up in Monte Carlo simulations to match real data through reweighting. By doing this, they can better understand and account for the impact of pile-up.

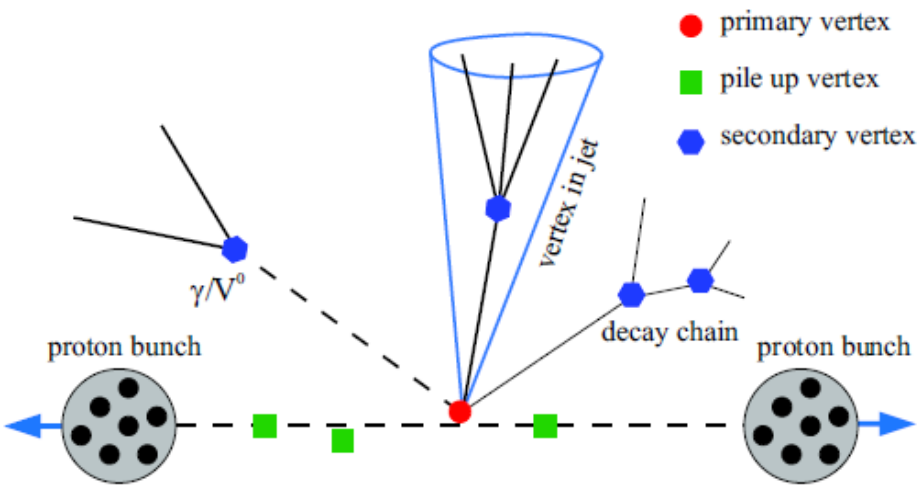


Figure 8. Vertex topologies in ATLAS, including primary (red), secondary (blue), and pile-up (red) vertices [7].

—

1.3.2 Timeline of LHC and ATLAS Data-Taking Runs. A brief overview of the LHC run timeline and the ATLAS data-taking is given below. Each operational period of the experiment is called a run and is characterized by higher center-of-mass collision energy, higher luminosity, and improved detector and software performance.

—

1.3.2.1 Run 1 (2010–2012). The first physics run of the LHC was Run 1. The LHC delivered proton-proton collisions at a center-of-mass energy of $\sqrt{s} = 7$ TeV in 2010 and 2011, and 8 TeV in 2012 with an integrated luminosity of $\sim 25\ fb^{-1}$ recorded for physics. The ATLAS detector was commissioned for physics, and its performance for tracking, calorimetry, muon detection, and triggers was established. The Higgs boson was discovered in 2012 by the ATLAS and CMS experiments at the LHC with a statistical significance of 5σ. Run 1 has proven the basic design of the ATLAS detector and has identified limitations regarding radiation-hard components, trigger rate, and tracking performance that can be addressed in subsequent upgrades.

—

1.3.2.2 Run 2 (2015–2018). During Run 2, the LHC was operating at a center-of-mass energy of $\sqrt{s} = 13$ TeV with an integrated luminosity of $\sim 140\ fb^{-1}$ recorded for physics, nearly doubling the energy available in Run 1. This allowed many physics processes to be studied in greater detail, including the Higgs boson, top quarks, electroweak processes, and searches for physics beyond the Standard Model.

A major upgrade of the ATLAS experiment for Run 2 was the installation of the Insertable B-Layer (IBL) around the beam pipe at a distance of about 50-60 mm from the interaction point. The IBL is one of the highest-pixel-density tracking detectors ever built and, together with improved vertexing, significantly improved the detector's performance. For the same reason as the increased luminosity in subsequent years, improvements to the trigger and track reconstruction software were significant.

—

1.3.2.3 Run 3 (2022–2026). During Run 3, the LHC reached the center-of-mass energy of $\sqrt{s} = 13.6$ TeV with an integrated luminosity of more than 300 fb^{-1} recorded for physics. Even though the collision energy increases only moderately, the higher luminosity (more than Run 1 and 2 combined) and more pile-up pose greater challenges.

The upgraded trigger and data acquisition system was deployed for full testing in Run 3, enabling the full exploitation of the ATLAS tracking system. Sophisticated real-time reconstruction and tracking techniques in a high-pile-up environment were validated and employed, in preparation for Run4 [26].

—

1.3.2.4 Long Shutdown 3 and Run 4 (HL-LHC Era). During the third long shutdown of the LHC (LS3), the collider will be upgraded to the High-Luminosity LHC (HL-LHC), with the goal of delivering an integrated luminosity of approximately 3–4 ab^{-1} [27], which is 10x that of Run 3. ATLAS will undergo major Phase-II upgrades, including the complete replacement of the Inner Detector with the all-silicon Inner Tracker (ITk) [28].

At HL-LHC, new aspects of tracking, triggers, and data processing have to be incorporated into the experimental analysis. In part, this will be done by more parallel computing. Also, hardware acceleration (FPGAs and GPUs) will play a role. Measurements of the Higgs coupling will have lower uncertainty. Also, rare processes in the Standard Model will be studied in detail. Eventually, new physics will also be searched with increased sensitivity.

—

1.3.3 The ATLAS Detector. The Inner Detector (ID) is the innermost tracking system in ATLAS and reconstructs the trajectories of charged particles produced in proton–proton collisions, which consists of pixel and strip detectors and Transition Radiation Tracker (TRT, which will be removed before Run 4). Operating in a 2-tesla solenoidal magnetic field enables precise measurements of charged-particle momenta via curvature. The trajectories and transverse momentum allow for accurate measurement of track parameters, particle identification, and vertex positions. The inner tracker is also used to calculate neutral-particle counts and missing transverse energy when combined with data from other detectors.

The calorimeter system surrounds the Inner Detector and is designed to measure particle energies through interactions with dense absorber materials. It is divided into electromagnetic and hadronic calorimeters. Electrons and photons disperse their energy by creating electromagnetic showers in electromagnetic calorimeters. Electrons and photons have enough energy to undergo bremsstrahlung (emit an additional photon) and pair production (create an electron-positron pair), respectively, triggering cascades until they lose enough energy to be absorbed, and the remaining energy is detected by the detectors. While gluons and quarks, due

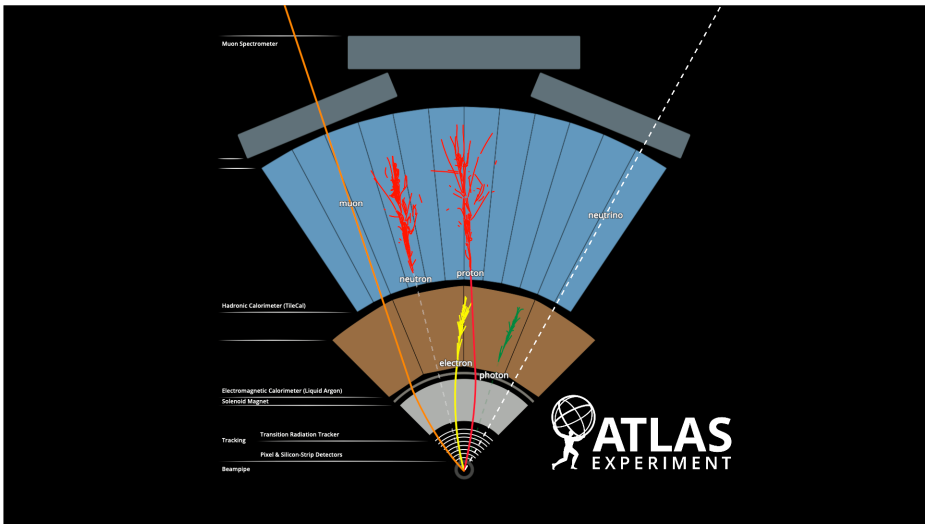


Figure 9. ATLAS detector slice with labeled subdetectors and particle visualizations [8]

to color confinement, tend to form bound states that produce collimated particle jets, they shower hadronically in the electromagnetic calorimeters and complete the process in the hadronization calorimeters.

The calorimeter system provides nearly full angular coverage and is essential for jet reconstruction, electron and photon identification, and the determination of missing transverse momentum. In addition to energy measurements, calorimeter information is used for particle identification and plays a key role in the trigger system.

The Muon Spectrometer forms the outermost detector system of ATLAS and is dedicated to identifying and measuring muon momentum. Muons have minimal energy loss as they pass through all the detectors, so they are detected by ionization in the Muon Chamber, and their overall momentum and energy are calculated from data in the Inner Detector and Muon Chamber.

Missing transverse energy (E_T^miss) is calculated from the transverse momentum symmetry of the initial proton collision. Since the beamline is in the

z direction, any imbalance in the transverse momentum of the detected particle indicates missing transverse energy in the other direction. These are mainly contributed by SM neutrinos and BDM particles, which weakly interact with detectors. As a result, all the detector results must be included in deriving the missing transverse energy.

—

1.3.4 Trigger and Data Acquisition System. The high collision rate delivered by the LHC far exceeds the rate at which events can be recorded for offline analysis. To address this challenge, ATLAS employs a trigger and data acquisition system that selects potentially interesting events in real time while rejecting most collisions.

The trigger system reduces the event rate through a multi-level selection process based on information from the detector subsystems. Trigger decisions are designed to maintain high efficiency in the physics processes of interest while operating within strict latency and bandwidth constraints. The data acquisition system then records the selected events for further processing and offline reconstruction. Together, the trigger and data acquisition systems enable ATLAS to efficiently exploit the LHC's physics potential.

1.4 ATLAS Run 4 Upgrade

In Run 4, the Large Hadron Collider will enter the High-Luminosity LHC (HL-LHC) phase, which is designed to significantly extend the ATLAS experiment's physics reach. The HL-LHC aims to deliver an integrated luminosity of approximately 3–4 ab^{-1} over its operational lifetime, corresponding to more than an order-of-magnitude increase relative to the datasets collected in earlier runs.

This increase will enable precise measurements of rare Standard Model processes and enhance sensitivity to physics beyond the Standard Model.

The higher luminosity of the HL-LHC will result in substantially more challenging experimental conditions. The instantaneous luminosity increases to an average pile-up level of up to $\langle\mu\rangle \sim 200$ interactions per bunch crossing. Such conditions will significantly increase detector occupancies, radiation exposure, and the complexity of event reconstruction. Maintaining the performance of tracking, vertexing, and triggering under these conditions requires major upgrades to the ATLAS detector systems.

A key component of the Phase-II upgrade program is the complete replacement of the current Inner Detector with a new all-silicon Inner Tracker (ITk). In Run 3, the primary tracker system of the ATLAS detector is the Inner Detector (ID), which consists of Pixel detectors, SemiConductor Trackers (SCT or strip detectors), and Transition Radiation Trackers (TRT) [11]. The Pixel and Strip detectors cover a pseudorapidity (η) range of $|\eta| < 2.5$ (TRT covers $|\eta| < 2.0$) with radiation tolerance designed for an integrated luminosity of 300–400 fb^{-1}.

For the High-Luminosity LHC (HL-LHC) upgrade, the ID will be replaced by the ATLAS Inner Tracker (ITK), the primary tracker system, which eliminates the TRT and replaces ID Pixel and Strip with ITK pixel (Inner) and ITK strip (outer) detectors. The ITK pixel will cover the pseudorapidity (η) range of $|\eta| < 4.0$, where the ITK strip covers $|\eta| < 2.7$. The designed radiation tolerance is upgraded to withstand an integrated luminosity of 4000 fb^{-1}. Moreover, the number of modules will be increased from 6000 to 28000; the number of channels will be increased from 100×10^6 to more than 5×10^9 in ITK.

In parallel, the ATLAS trigger and data acquisition system will be upgraded to cope with the increased event rates and data volumes expected during HL-LHC operation, as shown in Fig. 10. The upgraded trigger system adds L0-level processing for Calorimeters and the Muon System, as well as an Event Filter for Dataflow processing. The readout data rate increases from 100 kHz to 1 MHz, and the output data rate from 3 kHz to 10 kHz.

The ATLAS Phase-II upgrade program is therefore essential for sustaining detector performance and physics sensitivity throughout the HL-LHC era. The design choices and technological developments implemented during this upgrade phase directly address the challenges posed by high luminosity and pile-up [29] [30].

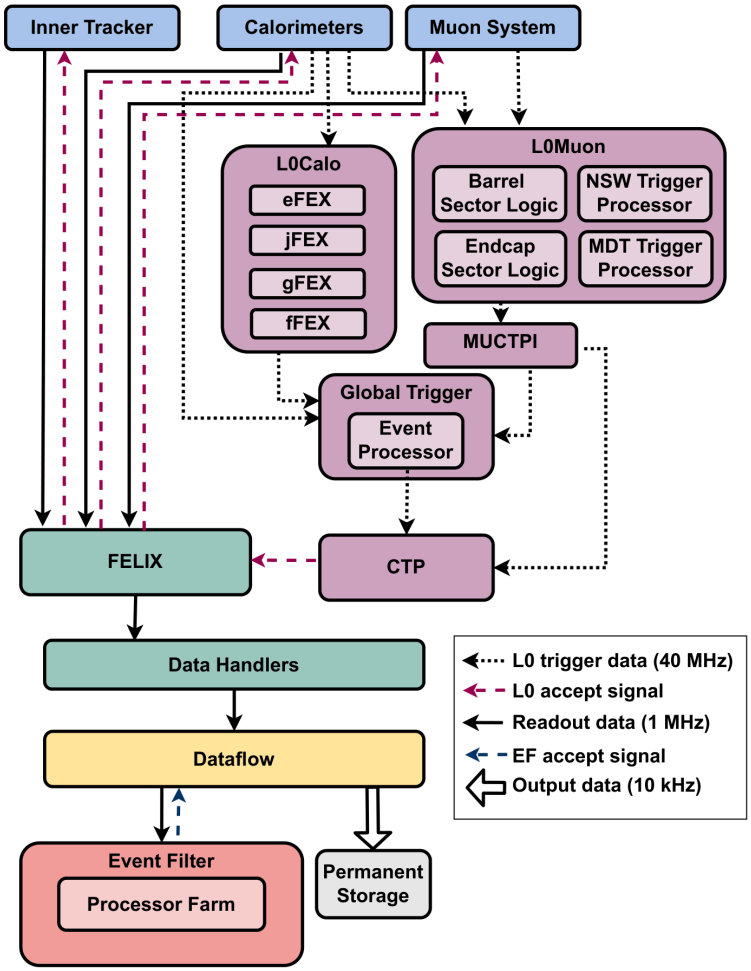


Figure 10. ATLAS Trigger and Data Acquisition System in Run 4 [9]

CHAPTER II

ATLAS EVENT FILTER (EF) TRACKING: STRIP CLUSTERING

2.1 Introduction

This report presents performance studies for the Event Filter (EF) Tracking project of the ATLAS experiment, part of its Phase-II upgrade program for the High-Luminosity LHC (HL-LHC). The HL-LHC pile-up conditions will produce an average of 200 inelastic proton–proton collisions per bunch crossing, and a new full-silicon Inner Tracker (ITk) [31, 32], designed to allow efficient tracking in such an environment, will be installed during the Phase-II upgrade. The high-pile-up conditions pose a significant challenge to the ATLAS TDAQ system, whose architecture and physics motivations are described in the Phase-II TDAQ TDR [33] and the Phase-II TDAQ TDR Amendment [34]. All the EF algorithms, including the EF Tracking ones, will run on a flexible, heterogeneous commercial system comprising CPU cores, possibly assisted by commodity accelerators such as GPUs or FPGAs. The rate at which events can be reconstructed for a given amount of computational hardware is a critical design factor for the EF system, with tracking historically the most computationally intensive reconstruction performed at the EF stage. The TDAQ design foresees that events are first processed by a hardware trigger (Level-0), which bases its decision on calorimeter and muon detector data. Accepted events are passed to the EF, which collects data from all detector readout systems at a maximum rate of 1 MHz. Following EF processing, the event acceptance rate is reduced to 10 kHz. Track reconstruction will play a critical role in the subsequent trigger decisions, helping to keep the EF output rate at a manageable level. It can be used to refine the selection of objects identified at Level-0, improve the precision of their kinematic measurements, and suppress

multi-object coincidences, for instance by requiring that associated tracks originate from the same primary vertex. Track reconstruction is, however, more challenging due to the high processing rate and the large hit density in the tracking detectors, which makes pattern recognition more computationally demanding. At the same time, the optimized layout of the ITk is expected to reduce the fake-track rate to a negligible level [31, 32].

To choose an EF Tracking design adapted to those challenges, the ATLAS Phase-II EF Tracking community embarked on a series of demonstrator cycles to study so-called tracking pipelines. In parallel, performance requirements for the EF tracking algorithms as well as the EF farm were produced, motivated by PPES studies aimed at the HL-LHC physics goals of ATLAS [35]. Following this, the design selection criteria and process were established. Both the requirements and criteria were reviewed and approved by a committee composed of various experts from within and outside of the ATLAS TDAQ community.

The studies presented in this report explore a possible EF Tracking design that uses GPU accelerators alongside conventional CPU processing. Tracking algorithms are put together to form a tracking pipeline. The pipeline referred to as C-000 is the default ITk track reconstruction which uses the legacy implementation of the tracking algorithms in ATHENA and serves as a reference for the comparisons of the various metrics. Several pipelines are described, with varying amounts of processing performed on GPU as indicated by the first digit: from G-0XX (minimal offloading) to G-2XX (full offloading).

2.1.1 Overview of GPU-based pipelines. The framework known as A Common Tracking Software (ACTS) [36] represents a robust, high-performance solution for track reconstruction in Particle Physics, usable across multiple

experiments. Designed with modularity, detector independence, and adaptability to contemporary computing architectures in mind, ACTS has been successfully integrated into the ATHENA software framework of the ATLAS experiment. It is currently slated to replace the existing offline tracking software for LHC Run 4 and subsequent operations. Furthermore, ACTS has been proposed as a key component for the Event Filter (EF) online track reconstruction, particularly within the C-100 and C-230 pipelines [37].

TRACCC [38] is a dedicated GPU-oriented research and development extension of ACTS, independently developed to address the stringent performance requirements of online track reconstruction in dense, high-rate detector environments. While TRACCC shares foundational algorithms, supporting libraries, and detector descriptions with ACTS, it is a separate piece of software designed to exploit the massive parallelism inherent in GPU hardware and to achieve portability across varying GPU hardware and software frameworks. This report focuses on the deployment of TRACCC within multiple types of GPU-based processing pipelines.

Within the pipelines denoted G-2X0, the entire track reconstruction sequence—including clustering, space point formation, seeding, track finding, and track fitting—is executed on the GPU. The CPU is used solely for transferring reconstructed tracks from GPU memory to host memory and for converting between TRACCC and ATHENA EDM. Other pipelines transition from GPU to CPU at different stages of the track reconstruction chain, executing the remaining reconstruction steps on the CPU. This GPU-CPU hybrid architecture leverages the strengths of both processing units to optimize overall performance, hypothesising that the most parallelizable and least branching stages—such as clustering and

seeding—benefit most from GPU acceleration. The remaining steps use the ACTS algorithms in a workflow equivalent to that of the C-100/C-230 pipelines. The hybrid pipelines differ in which stages of track reconstruction are offloaded to the GPU: G-0X0 pipelines offload only the clustering step, G-1X0 pipelines offload both clustering and track seeding, G-2X5 offload clustering, seeding and track finding. Since my study focuses on a GPU-based strip clustering algorithm, this paper will focus on performance and efficiency in the G-080 pipeline.

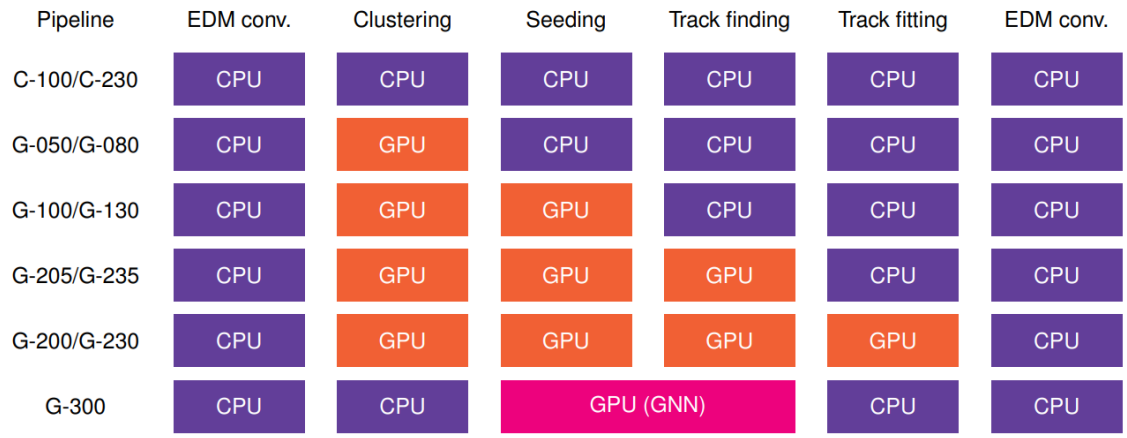


Figure 11. Overview of the reconstruction pipelines, including the G-050, G-130, and G-200 pipelines discussed in this thesis.

2.1.1.1 Inner Tracker (ITK) Strip Detectors.

For Inner Tracker (ITK) strip detectors, there are about 18,000 modules and 60 million strip channels distributed in the central region known as the Barrel, and two lateral cylinders called End-Caps (EC) [11].

The ITK-Strip Barrel is composed of staves, each of which hosts 14 rectangular modules on each side, as shown in Fig. 12. Each module has a geometry of 97 mm × 97 mm. There are a total of four rows (2 rows of short-strip sensors and 2 rows of long-strip sensors), each containing 1280 strips with a 75.5

μm pitch between sensors [39]. The two inner layers of short strips have a length of 24.1 mm, while the two outer layers of long strips are 48.3 mm long.

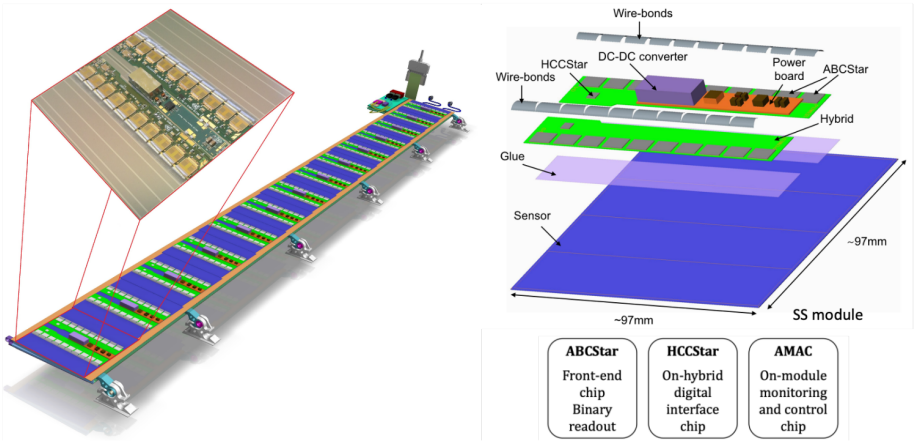


Figure 12. Stave with 14 Short Strip modules. The sensor consists of two hybrids and one power board [10].

The End-caps (EC) are two cylinders, each with six disks, as shown in Fig. 13. The EC modules are mounted on Petals. There will be 32 petals per disk, for a total of 384 petals and 6912 modules [40]. Due to its radial shape, the non-uniform strip lengths range from 15 to 60 mm, and the sensor pitch is 70–80 μm with a spatial resolution of about 20 μm and a time resolution around 3 ns.

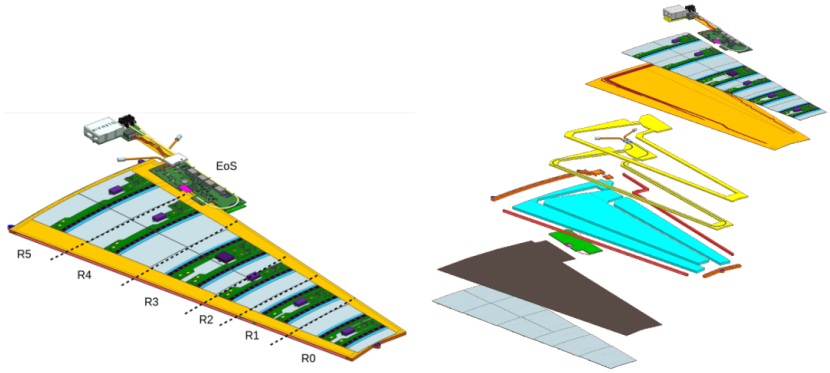


Figure 13. A view of the end-cap petal with six silicon modules and an EoS card placed on each side [11].

2.1.1.2 Motivation for GPU Implementation.

Silicon strip clustering exhibits intrinsic parallelism. Clusters are formed independently within each detector module, and individual strip hits can be processed concurrently when searching for neighboring channels above threshold. This structure makes the algorithm well-suited for GPU execution, where thousands of lightweight threads can operate simultaneously.

However, achieving efficient GPU performance requires more than simply parallelizing loops. Memory layout, coalesced access patterns, thread mapping strategies, and synchronization between neighboring strips must be carefully designed to avoid performance bottlenecks. Additionally, the algorithm must reproduce the clustering behavior of the reference Athena implementation to ensure consistency in downstream tracking performance.

The motivation for implementing strip clusterization on GPUs within `traccc` is therefore twofold:

- To reduce the computational latency of clustering in high-occupancy environments.
- To establish a validated GPU-based tracking workflow compatible with ATLAS software standards.

Demonstrating physics equivalence while achieving computational gains is essential for future integration into trigger or offline reconstruction chains.

2.1.2 Strip clustering algorithm.

The strip clusterization is performed by means of a Connected Component Analysis (CCA) algorithm. The readout of the ATLAS strip detectors is binary, i.e. hit or no-hit. A charged particle crossing a layer of a silicon sensor generates electron-hole pairs which

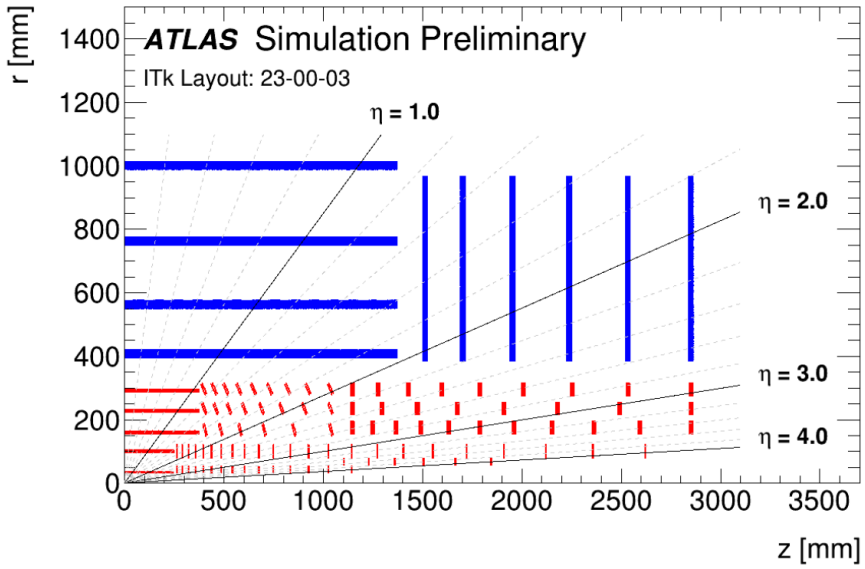


Figure 14. The layout of the ATLAS ITK, where the red represents the pixel detectors, and the blue represents the strip detectors (horizontal blue lines are barrel, and vertical are annulus) [12].

drift to the readout strips and are collected by the adjacent readout strips. As a result, the charge generated by a charged particle is distributed among a number of adjacent readout strips. Therefore, a charged particle crossing a layer of a silicon detector is detected as a cluster of adjacent fired readout strips. A set of adjacent fired readout strips is called a cluster within this algorithm. The uncorrected cluster position, or centroid (x_{cluster}) of a cluster, is calculated using the following equation:

$$x_{\text{cluster}} = \frac{x_{\text{first}} + x_{\text{last}}}{2} \tag{2.1}$$

where x_{first} and x_{last} are the local spatial coordinates of the first and last strips in the cluster.

The strip detectors in ATLAS are mounted inside a 2 T solenoid, resulting in the electron-hole pairs generated by charged particles passing through the sensors being subject to the Lorentz force, $\vec{F} = q\vec{E} \times \vec{B}$. This causes the charge carriers to

drift at an angle θ_L, known as the Lorentz angle, relative to the electric field lines. As a result of this angled drift, the collected charge distribution is systematically shifted along the transverse plane. To recover the particle's true intersection point with the sensor, a correction must be applied to the cluster centroid. The magnitude of this Lorentz shift (Δx_L) evaluated at the mid-plane of the sensor is given by:

$$\Delta x_L = \frac{d}{2} \tan(\theta_L) \tag{2.2}$$

where d is the active thickness of the silicon sensor. The corrected local x-coordinate is thus:

$$x_{\text{corrected}} = x_{\text{cluster}} - \Delta x_L \tag{2.3}$$

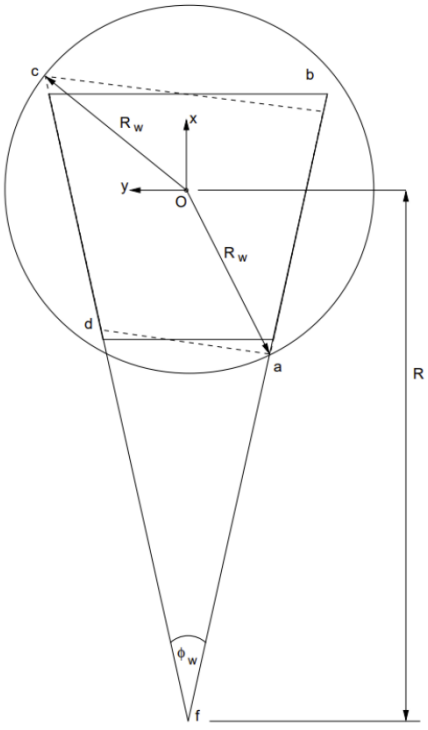
The sign of Δx_L is dependent on the detector module's orientation with respect to the magnetic field.

Once the Lorentz shift corrects for the $E \times B$ drift of charge carriers in the magnetic field, the hit coordinates are evaluated in the **Beam Frame (BF)**. For the ITk strip endcaps, which utilize annulus-shaped modules, as shown in Figure 15b, these coordinates must subsequently be shifted into the **Strip Frame (SF)** due to its shape.

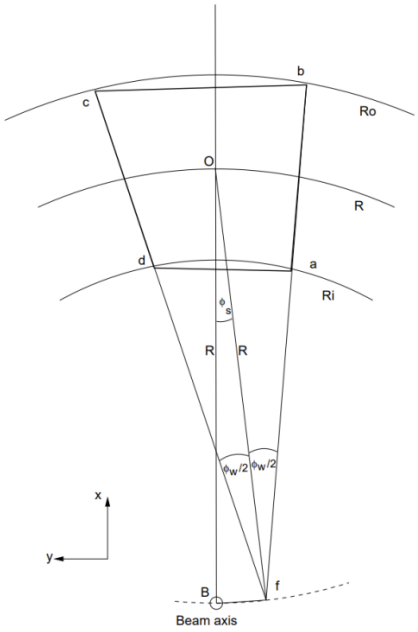
The transformation shifts the origin of the coordinate system from the beamline to the specific focus point of the annulus strips (f). In Cartesian coordinates, this involves a translation to the module origin, a rotation by the stereo angle ϕ_s, and a final translation to the strip focus.

Mathematically, this transformation is expressed as:

$$\begin{pmatrix} x_{SF} \\ y_{SF} \end{pmatrix} = \begin{bmatrix} \cos(-\phi_s) & -\sin(-\phi_s) \\ \sin(-\phi_s) & \cos(-\phi_s) \end{bmatrix} \begin{pmatrix} x_{BF} - R \\ y_{BF} \end{pmatrix} + \begin{pmatrix} R \\ 0 \end{pmatrix} \tag{2.4}$$



(a) Definition of the trapezoidal modules used in the SCT endcaps [41].



(b) Definition of the annulus modules used in the ITK Strip endcaps [42].

where R is the radial distance to the module origin.

2.1.3 Integration with the `Traccc` framework. The input data include the strip ID (stripID) and the number of fired strips (nFiredStrip). For instance, if stripID is zero and nFiredStrip is 3, then the stripID is 0, 1, 2 as input to the strip clustering algorithm. For strip modules, a digitization configuration is required to log the cell information to their corresponding modules. The configuration includes the volume, layer, sensitive information, module rows and columns, width, and length. Since strip modules are one-dimensional, the barrel has only one module column, and the module rows are the number of cells in that module. For annulus modules, due to their parabolic shape, the module rows and width are recorded as the number of cells and theta relative to the center in the beam frame, where the module columns and length are one and the radius from the center. After clustering, the Lorentz shift is applied to the annulus modules, and the local positions are then transformed from the beam frame to the strip frame.

2.2 Results and Discussion

2.2.1 Cluster comparison with CPU. Fig. 16 demonstrates the residuals of local position in x, y between TRACCC and ATHENA (CPU) for both barrels and endcaps; the central bin at 0 indicates the two outcomes are consistent. The accuracy for the residual is within $\mathcal{O}(10^{-10})$ mm. After running the full reconstruction pipeline, the average times for each using the G-080 pipeline for $t\bar{t}$ events at $\langle\mu\rangle = 140$ and $\langle\mu\rangle = 200$ are shown in the table. 1. Since both pixel and strip information are fed into the clustering algorithm step, the combined clustering times are 0.5 ms and 0.7 ms, respectively. For further validation, Fig. 17 and Fig. 18 illustrate a match in the number of strip clusters with η dependence and global positions (in x, y, z) between TRACCC and ATHENA (CPU).

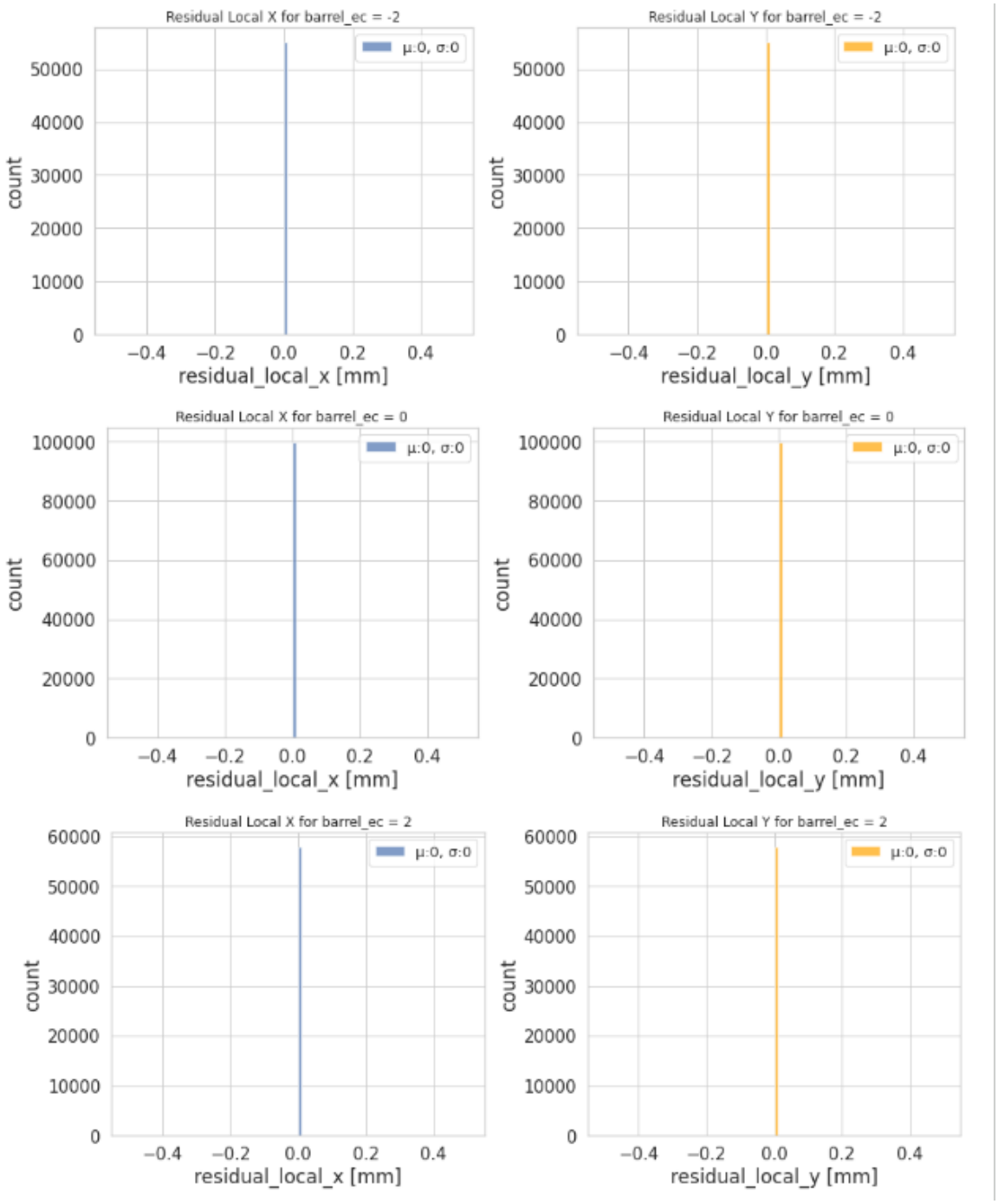
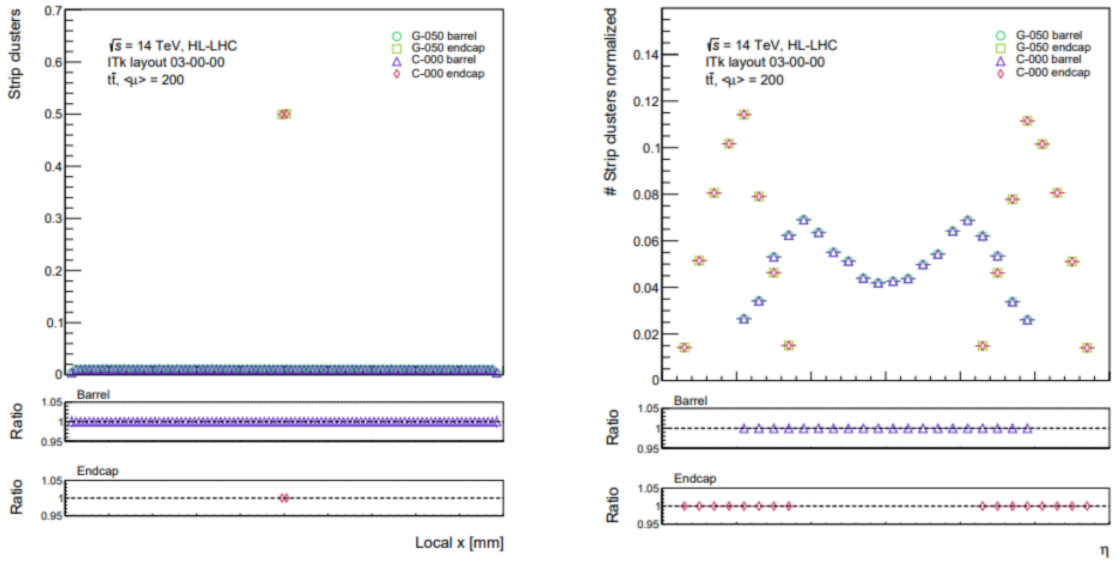


Figure 16. Residue of Local Position (x, y) between TRACCC and ATHENA (CPU) outcome, where top and bottom plots are annulus, and the middle plots are barrel modules. The accuracy is within $\mathcal{O}(10^{-10})$ mm.

Generic Step	**Step**	$\mu = 140$		$\mu = 200$	
		Timing [ms]	[HS23.s]	Timing [ms]	[HS23.s]
RDO Conversion	RDO to traccc	121	4.2	159.0	5.6
GPU Transfer	Host to Device Transfer	1.1	0.0	1.2	0.0
Clustering	Clustering Algorithm	0.5		0.7	
Spacepoint Formation	Measurement Sorting	1.9		2.5	
	Cluster Conversion	35.9	1.3	47.1	1.7
Seeding	Seeding Algorithm	85.4	3.0	138.5	4.9
Track Finding	Track Finding Algorithm	236.5	8.3	336.7	11.8
Acts to xAOD Convers.	Conversion Algorithm	11.7	0.4	16.1	0.6
GPU Transfer	Device to Host Transfers	1.3	0.0	2.2	0.1
Total CPU		493.0	17.3	700.8	24.6
Of which: GPU overhead		159.3	5.6	209.5	7.4
Total GPU		2.4		3.1	
Accelerator Concurrency Factor		0.52		0.53	
Total GPU with Concurrency		1.3		1.6	

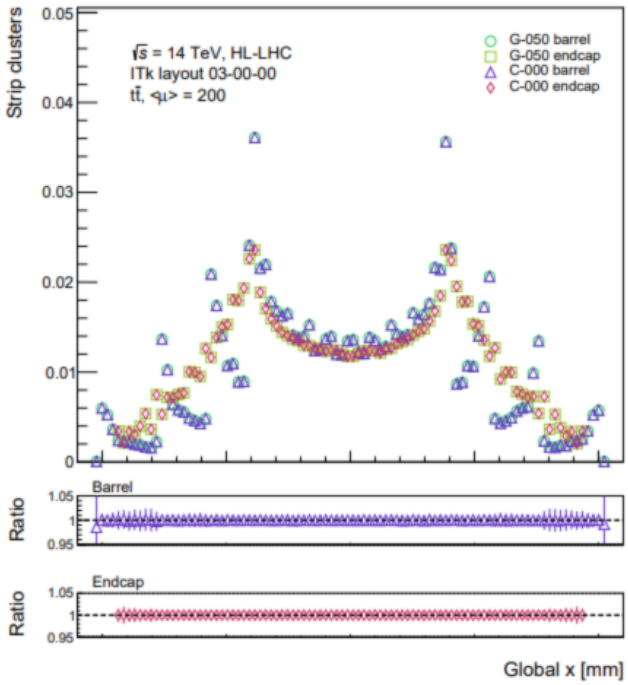
Table 1. Average timing of the different steps of track reconstruction using the G-080 pipeline for $t\bar{t}$ events at $\langle\mu\rangle = 140$ and $\langle\mu\rangle = 200$. Since both pixel and strip clustering were sent to the GPU, the clustering timing includes both. HS23 refers to HEPScore23, a CPU performance benchmark used to evaluate and quantify computing power.



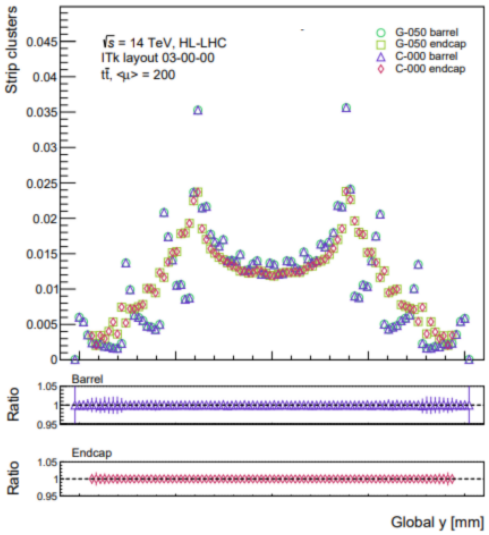
(a) Local position distribution.

(b) Number of strip clusters vs. η.

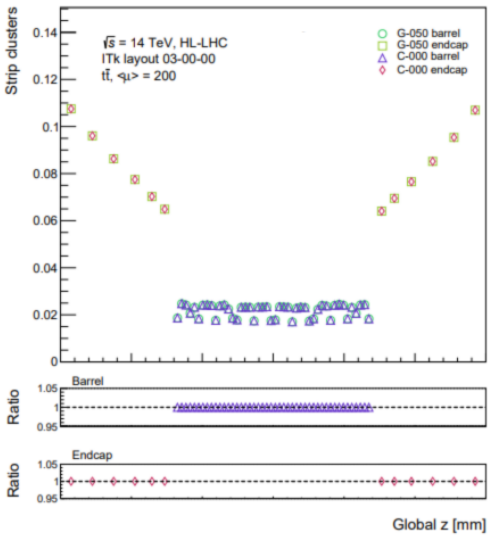
Figure 17. Validation of strip cluster local coordinates and η dependence.



(a) Global x position.



(b) Global y position.



(c) Global z position.

Figure 18. Global coordinate distributions for the strip clusters.

2.2.2 Summary of EF Tracking validation.

The plots in the results show strong agreement between TRACCC and ATHENA (CPU), indicating that the strip clustering algorithm in TRACCC is functioning correctly and reliably. These results were included in the EF Tracking "technology choice" process; ATLAS has chosen a heterogeneous form using CPU + GPUs, based on the balance of risks and opportunities across the technologies.

CHAPTER III

ATLAS: SIGNAL OPTIMIZATION OF A SEARCH FOR HIGGS DECAYS TO DARK PHOTONS USING ATLAS RUN 3 DATA

3.1 Title

Search for dark photons from Higgs boson decays in the gluon-gluon fusion channel in proton-proton collisions at $\sqrt{s} = 13.6$ TeV with the ATLAS detector

3.2 Disclaimer

This chapter will be published as a co-authored paper; the credit belongs to the ATLAS Collaboration. See reference [43] for a link to the latest draft to publication.

3.3 Abstract

This paper presents a search for semi-visible Higgs boson decays in final states with a photon (γ) and missing transverse momentum p_T^{miss}. The analysis is optimised for the gluon-gluon fusion production channel and exploits a novel trigger deployed in 2023, with reduced thresholds down to 50 GeV on the photon transverse momentum (p_T^{γ}) and 70 GeV on the p_T^{miss}, in combination with a selection on the transverse mass of the p_T^{miss}-γ system (m_T) above 80 GeV. The results are interpreted in terms of Higgs boson decays into a γ and a dark photon γ_d ($H \to \gamma\gamma_d$). The analysis is performed using 135 fb^{-1} of Run 3 data collected by ATLAS in 2023 and 2024. A boosted decision tree is used to identify events with misreconstructed primary vertices, which can affect the p_T^{miss} calculation. Data-driven methods are employed to estimate the backgrounds from jets and electrons misidentified as photons, while the backgrounds with genuine photons are taken from Monte Carlo simulations, normalised to data in control regions with muons. A binned maximum-likelihood fit to the m_T distribution is performed to evaluate

the compatibility of the observed data with the Standard Model expectation. No significant excess is observed over the Standard Model prediction, and an observed (expected) upper limit on the branching ratio of $H \rightarrow \gamma\gamma_d$ of 1.4% (1.2%) is obtained at 95% confidence level. Combining this result with previous Run 2 searches improves the observed (expected) upper limit to 0.9% (0.9%).

3.4 Introduction

3.4.1 Motivation for Hidden Sectors. While Section 1.2 gives a brief overview of the astrophysical evidence for dark matter, the Standard Model offers no viable particle candidate. This motivates the hypothesis of a Dark Section (DS), in which the dark photon (γ_d) is the gauge boson of an additional $U(1)_D$ gauge group. Strong motivations for the search for this particle arise from its potential contribution in solving the small-scale structure formation problems [44] [45], as well as being a possible source for the Sommerfeld enhancement of DM annihilation required to explain the PAMELA-Fermi-MS2 positron anomaly in terms of DM [46], or making asymmetric DM scenarios viable [47].

—

3.4.2 Dark Photon. The dark photon, denoted A'_μ, is associated with a new $U(1)_D$ gauge symmetry.

The decay of the Higgs boson into a photon and a dark photon, $H \rightarrow \gamma\gamma_d$ provides an interesting production channel for this BSM particle. The study focuses on a massless dark photon, which cannot directly couple to Standard Model (SM) particles [48]. In this case, the kinetic mixing between the γ_d and the photon can be tuned away through a rotation of the gauge fields, and the γ_d can interact with ordinary matter only through operators of dimension higher than four [48]. The Higgs boson can decay through a loop interaction involving additional (pseudo-

)scalar BSM messenger fields, which couple both to the SM and the DS [49, 50], as shown in Fig. 19. Thanks to the non-decoupling properties of the Higgs boson, and depending on the parameters of the model, a branching ratio (BR) of $H \to \gamma\gamma_d$ of a few percent can be allowed [51, 52].

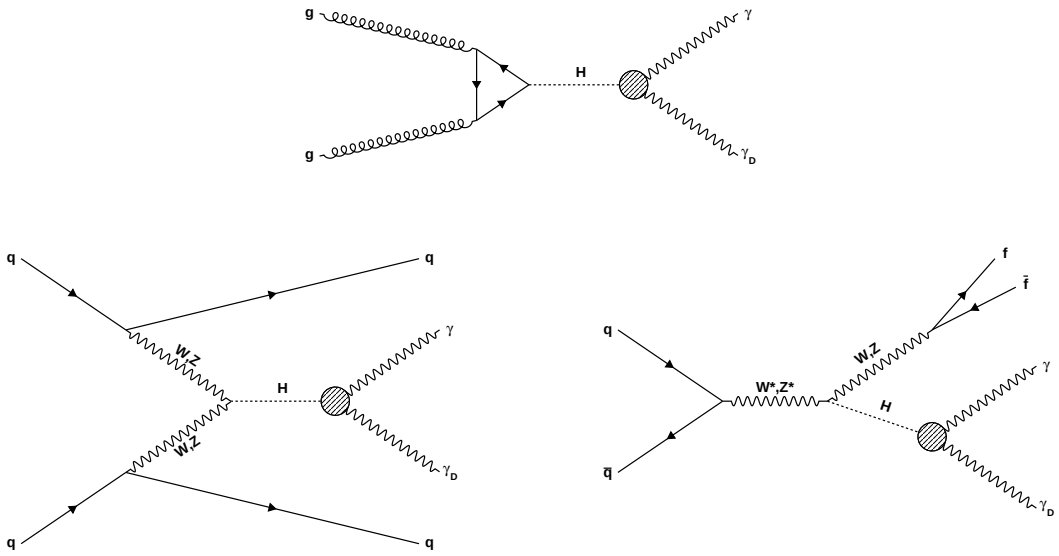


Figure 19. Feynman diagram illustrating the Higgs boson production via gluon-gluon fusion process (top) and vector-boson fusion (VBF) and Higgsstrahlung (VH) processes (bottom left and right), all followed by the decay into a photon and a dark photon ($H \to \gamma\gamma_d$). The hatched circle in the $H\gamma\gamma_d$ vertex represents the interaction through messenger fields.

Searches for the $\gamma + E_{\mathrm{T}}^{\mathrm{miss}} + X$ signature have been widely performed at the LHC by the ATLAS and CMS experiments, in both the vector boson fusion (VBF) production mode and associated production with a Z boson (ZH) [53–60]. A combination of ATLAS results in the ZH and VBF channels currently provides the most stringent limits, excluding $\mathrm{BR}(H \to \gamma\gamma_d) > 1.3\%$ (1.5% expected) at 95% CL. This result is based on an integrated luminosity of $139\,\mathrm{fb}^{-1}$ collected during LHC Run 2 at $\sqrt{s} = 13$ TeV [61].

Though these two production modes provide clean final states, the gluon-gluon fusion one (ggF) is an order of magnitude larger in cross-section than the VBF channel. This channel has been explored by CMS [59], but not yet by ATLAS – though the inclusive signature with a single photon has been pursued in the context of other exotic models [55]. One challenge is that this kind of signature was not accessible via the available triggers due to their high photon p_{T} or $E_{\mathrm{T}}^{\mathrm{miss}}$ thresholds. Developments in the trigger between Run-2 and Run-3 led to the implementation of a lower threshold trigger, which increases the acceptance of ggF events by approximately a factor of two, while keeping the trigger rate under control.

The analysis presented in this paper targets the $H \rightarrow \gamma\gamma_d$ decay in the ggF production channel for the first time in ATLAS, retaining sensitivity also to the VBF, ZH and WH channels. The analysis is based on the LHC Run-3 proton–proton collisions data at $\sqrt{s} = 13.6$ TeV recorded by the ATLAS experiment in 2023 and 2024, corresponding to an integrated luminosity of 134.6 fb^{-1} .

3.5 Data and MC samples

3.5.1 Data samples. The data used in this analysis were collected in 2023 and 2024. The used Good Run List is

Year	**GRL String**	**Lumi [fb^{-1}]**
2023	data23_13p6TeV.periodAllYear_DetStatus-v133-pro31-11_MERGED_PHYS_StandardGRL_All_Good_25ns	25.2
2024	data24_13p6TeV.periodsEtoO_DetStatus-v130-pro36-08_MERGED_PHYS_StandardGRL_All_Good_25ns	109.4

Table 2. Summary of the Good Run Lists (GRL) and integrated luminosities used for the Run 3 analysis.

for a total integrated luminosity of 134.6 fb^{-1} , with an uncertainty of 2% [62].

3.5.2 MC samples. The MC samples were processed with p-tag p6697, which labels the specific ATLAS production campaign and the processing configuration used to generate the data.

The signal samples were showered from common Higgs Les Houches Event (LHE) samples generated using Powheg. The decay process used in the shower was implemented with Pythia [63–65]. The signal sample paths are shown in table 2.

The primary backgrounds for the analysis include processes with a true photon in the final states and genuine E_T^{miss}. These samples include: $Z\gamma$ and $W\gamma$, where the vector boson can decay to a lepton that is not reconstructed or to neutrinos. Additional background processes arise from fake photons due to misidentified jets or electrons, and/or fake E_T^{miss}. The background from jets or electrons misidentified as photons is mainly given by $Zjets$, $Wjets$, di-jets, and $\gamma jets$ with a fragmentation photon. The $Zjets$, di-jets, and $\gamma(frag)jets$ events are also characterized by fake E_T^{miss} due to mis-measured or not reconstructed jets. Finally, $\gamma jets$ with direct photon ($\gamma(direct)jets$) enter the analysis regions exclusively due to the presence of fake E_T^{miss}.

The list of MC samples used in this analysis is presented in the Appendix tables in Chapter A. As detailed later, MC simulations are ultimately employed only for true photon backgrounds (including the $\gamma(direct)$ jets), while the contribution from events with fake photons is estimated using data-driven methods. The W/Z MC samples are used as part of the jet-fakemethod and therefore listed in the following tables, while $\gamma(direct)jets$ and di-jets have been used exclusively for preliminary studies and initial optimization of the analysis selection and are not reported here.

3.6 Physics object reconstruction and identification

Physics objects used in this analysis are reconstructed following standard ATLAS procedures. Photon candidates are reconstructed from topological clusters in the electromagnetic calorimeter and calibrated using an energy calibration chain, and are required to satisfy tight identification criteria based on shower-shape variables together with isolation requirements designed to suppress hadronic backgrounds [66]. Muons are reconstructed by combining tracks from the inner detector and the muon spectrometer, and are selected using quality and isolation working points that ensure high efficiency while suppressing non-prompt backgrounds [67]. Electrons are formed by matching inner-detector tracks to electromagnetic calorimeter clusters and are identified using likelihood-based discriminants exploiting shower shapes, track quality, and track–cluster matching observables [68]. Jets are reconstructed using the anti-k_t algorithm with radius parameter $R = 0.4$ applied to particle-flow or topological calorimeter inputs, and are calibrated through simulation-based and in situ corrections, with additional pile-up mitigation techniques such as jet-vertex tagging applied [69]. To avoid double-counting of detector signatures, reconstructed objects are subjected to an overlap-removal procedure that resolves ambiguities among nearby photons, leptons, and jets using a fixed priority scheme [70]. The missing transverse momentum, $\vec{p}_{\mathrm{T}}^{\,\mathrm{miss}}$, is computed as the negative vector sum of the transverse momenta of all reconstructed baseline objects, supplemented by a track-based soft term associated with the primary vertex to reduce pile-up sensitivity [71]. These definitions ensure a consistent and well-validated reconstruction of final-state objects across ATLAS analyses.

Table 3. Electron selection criteria.

Feature	Criterion
Object quality	Not from a bad calorimeter cluster (`BADCLUSELECTRON`)
Energy calibration	`es2024_Run3_v0` (ESModel)
Pseudorapidity range	$(\lvert\eta\rvert < 1.37) \quad \lvert\rvert \quad (1.52 < \lvert\eta\rvert < 2.47)$
Transverse momentum	$p_{\mathrm{T}} > 10$ GeV
Track to vertex association	$\lvert d_0^{\mathrm{BL}}(\sigma)\rvert < 5$ $\lvert\Delta z_0^{\mathrm{BL}} \sin\theta\rvert < 0.5$ mm
Baseline	
Identification	`LooseAndBLayerLLH`
Selected	
Identification	`TightLLH`
Isolation	`Tight_VarRad`

Table 4. Jet reconstruction criteria.

Feature	Criterion
Algorithm	`Anti-kt`
R-parameter	0.4
Input constituent	PFlow
Calibration configuration	`AntiKt4EMPFlow_MC23a_PreRecR22_Phase2_CalibConfig_ResPU_EtaJES_GSC_241208_InSitu.config`
Jet cleaning	`LooseBad`
p_T	$p_{\mathrm{T}} > 20$ GeV
$\lvert\eta\rvert$	< 4.5
JVT Working point	`FixedEffPt`
fJVT Working point	`Loose`

Table 5. Muon selection criteria.

Feature	Criterion
Object quality	Bad Muon Veto
p_{T} cut	$p_{\mathrm{T}} > 10$ GeV
$\lvert\eta\rvert$ cut	< 2.7
d_0 significance cut	3
z_0 cut	0.5 mm
Baseline	
Identification working point	`Medium`
Selected	
Identification working point	`Medium`
Isolation working point	`PflowLoose_VarRad`

Table 6. Overlap removal criteria.

Reject	Against	Criteria
Electron	Electron	shared track, $p_{\mathrm{T},1} < p_{\mathrm{T},2}$
Tau	Electron	$\Delta R < 0.2$
Tau	Muon	$\Delta R < 0.2$
Muon	Electron	is Calo-Muon and shared ID track
Electron	Muon	shared ID track
Photon	Electron	$\Delta R < 0.4$
Photon	Muon	$\Delta R < 0.4$
Jet	Electron	$\Delta R < 0.2$
Electron	Jet	$0.2 < \Delta R < 0.4$
Jet	Muon	`NumTrack` < 3 and (ghost-associated or $\Delta R < 0.2$)
Muon	Jet	None
Jet	Tau	$\Delta R < 0.2$
Jet	Photon	$\Delta R < 0.4$

Table 7. Photon selection criteria.

Feature	Criterion
Object quality	Not from a bad calorimeter cluster (`BADCLUSPHOTON`)
Photon cleaning	`passOQquality`
Pseudorapidity range	$(\lvert\eta\rvert < 1.37) \quad \lvert\rvert \quad (1.52 < \lvert\eta\rvert < 2.37)$
Energy calibration	`es2024_Run3_v0` (ESModel)
Baseline photons	
Transverse energy	$p_{\mathrm{T}} > 25$ GeV
Identification	`Tight`
Selected photon	
Transverse energy	$p_{\mathrm{T}} > 50$ GeV
Identification	`Tight`
Isolation	`TightCaloOnly`

3.7 Event selection

3.7.1 Trigger. The analysis uses a trigger implemented in 2023. The trigger requires a single photon at 26 GeV at L1 – which is shared with the single-electron L1 item. The HLT is a multi-object trigger that requires a 50 GeV tight ID photon (g50), 40 GeV of cell E_T^{miss} (xe40_cell) and 70 GeV of "pfopufit" E_T^{miss} (xe70_pfopufit). There transverse mass computed between the photon and the E_T^{miss} is defined using the expression: $m_T = \sqrt{2E_T^{\gamma}E_T^{miss}(1 - cos(\Delta\phi))}$. The trigger requires that: $m_T > 80$ GeV be applied (`80mTAC`).

This trigger is consistently applied in all the analysis regions, which are generally characterized by signatures allowing reasonable trigger acceptance: $1\mu + \gamma$, $2\mu + \gamma$, 1 non-isolated $\gamma + E_T^{miss}$, $1e + E_T^{miss}$. For the muon-CRs, it is possible to apply the analysis trigger taking advantage of the fact that muons are not included in the trigger-level E_T^{miss} computation. The most critical final state is $1e + E_T^{miss}$: in this case, an OR of multiple single-electron triggers and the analysis trigger is applied.

3.8 Signal region optimization

The set of rectangular cuts resulting from the previous optimization is the following:

Preselections:

- Analysis trigger: `HLT_50ightz40_eLLz70_fopupfit8_mTAC_LeEM26M`
- $N_\gamma = 1$, with N_γ the number of selected photons;
- $N_{\text{leptons}} = 0$, for baseline leptons;
- $N_{\text{jet, central}} \leq 3$;
- $p_T^{\gamma} > 50$ GeV;
- $E_T^{\text{miss}} > 100$ GeV;
- $m_T(E_T^{\text{miss}}, \gamma) > 80$ GeV;

Additional selections:

- $\text{BDT}_{\text{score}}^{\text{vertex}} > 0.1$;
- E_T^{miss} significance > 6;
- $\Delta E_T^{\text{miss}} > -10$ GeV;
- $\Delta\phi(E_T^{\text{miss}}, E_T^{\gamma}) > 1.25$;
- $\Delta\phi(E_T^{\text{miss}}, E_T^{\text{jet}}) < 0.75$;
- $\Delta\phi(j_1, j_2) < 2.5$;
- $|\eta_\gamma| < 1.75$;

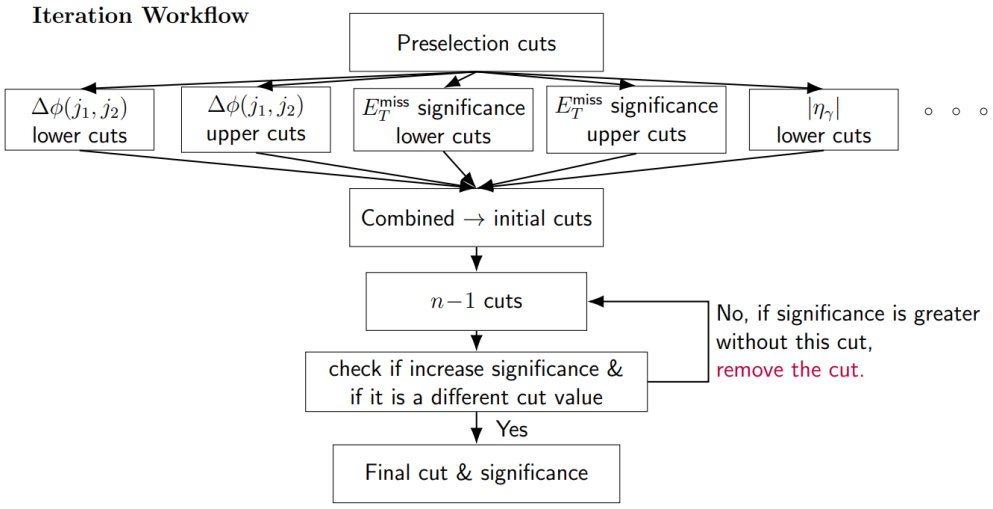


Figure 20. Iteration workflow for optimizing the cut set using n-1 studies and significance checks.

3.8.1 N-1 iteration method. The iteration process, demonstrated in figure 20, determines the optimized cuts for the additional selections. After applying preselection cuts, it imposes lower and upper bounds on the key variables, denoted c_i for clarity, based on their ROC curves. If either an upper/lower cut does not improve significance, we will skip the cut for this variable, but it will be reconsidered and iterated in a later process. Combining all the cuts becomes our

Table 8. Preselections and basic-cut comparison between the Internal Note and Optimized Selections

Selection	**Internal Note**	**Optimized Selections**
	Preselections	
Analysis trigger	`HLT_50ightz40_eLLz70_fopupfit8_mTAC_LeEM26M`	
Number of photons N_γ	$= 1$	
Number of leptons N_{leptons}	$= 0$ (baseline leptons)	
Central jets $N_{\text{jet, central}}$	≤ 3	
Photon transverse momentum p_T^γ	> 50 GeV	
Missing transverse energy E_T^{miss}	> 100 GeV	
Transverse mass $m_T(E_T^{\text{miss}}, \gamma)$	$100 < m_T < 140$ GeV	
	Additional selections	
$\text{BDT}_{\text{score}}^{\text{vertex}}$	> 0.1	> 0.1
E_T^{miss} significance	> 6	> 7
Photon pseudorapidity $\lvert\eta_\gamma\rvert$	< 1.75	< 1.75
$\Delta\phi(E_T^{\text{miss}}, E_T^\gamma)$	> 1.25	> 1.25
ΔE_T^{miss}	> -10 GeV	> -25 GeV
$\Delta\phi(j_1, j_2)$ (central jets)	< 2.5	< 2.5
$\Delta\phi(E_T^{\text{miss}}, \text{jet})$	< 0.75	< 0.75
balance	—	> 0.90
$S/\sqrt{B}$	2.475	2.701

initial cuts of the variables. Then it performs n-1 cuts: for each cut c_i, apply all the cuts except c_i and calculate the n-1 significance. Choose the cut value of c_i that maximizes the significance, and repeat the process for the next c_{i+1}. If the n-1 significance is greater without the cut, we remove the cut. In the next iteration, it will reconsider the entire list of cut variables and cut values, including those previously dropped. We finalize the optimized cuts and significance if none of the chosen cuts change, and there is no further improvement in significance in one iteration.

After checking n-1 plots of each variable, we optimized the cuts to:

The balance variable is defined as

$$\text{balance} \equiv \frac{E_T^{\text{miss}} + p_T^{\text{leading}\,\gamma}}{\sum_{\text{central jets}} p_T^j}. \tag{3.1}$$

Compared to the internal note cuts, the lower cut of E_T^{miss} significance change from 6 to 7, the ΔE_T^{miss} alters from -10 GeV to -25 GeV, and we add a lower cut of 0.90 for balance.

With the improved optimized cuts, we increased the simple significance $\frac{S}{\sqrt{B}}$ from 2.475 to 2.701.

3.8.2 Statistical method. The combination is done using a combined likelihood function, i.e. the product of the likelihoods for the individual channels times the product of the likelihoods for the final observables in each of the analysis categories within a single analysis.

In the above combination, the common parameter of interest (POI) for all channels to be combined is the ratio $H \to \gamma\gamma_d$ branching ratio, denoted by μ. The systematic uncertainties are modeled as nuisance parameters $\boldsymbol{\theta}$, which are treated as Gaussian variables. They represent information from auxiliary measurements and parameterize the uncertainty of that information, i.e. the (different) uncertainty of a systematic to mimic the signal in the current combination. In the fit across the various backgrounds, the corresponding normalization, $\boldsymbol{\kappa}$, is also treated as a free parameter without any constraints. This parameter is used to achieve the best possible agreement with the data in the corresponding CR(s) for the background shapes.

The combined likelihood can be written as [72]

$$\mathcal{L}\left(\text{data}|\mu, \boldsymbol{\kappa}, \boldsymbol{\theta}\right) = \prod_{c=1}^{N_{\text{cats}}} \mathcal{L}_c\left(\text{data}|\mu, \boldsymbol{\kappa}, \boldsymbol{\theta}\right) \prod_{k=1}^{N_{\text{cons}}} \mathcal{G}\left(\tilde{\theta}_k|\theta_k\right), \tag{3.2}$$

where N_{cats} is the number of categories, N_{cons} is the number of constrained NPs, $\tilde{\theta}_k$ is the global observable corresponding to θ_k, c is the index for the event categories, k is the index for the constrained NPs, and $\mathcal{G}$ represents a Gaussian distribution.

The likelihood for a given category $\mathcal{L}_c$ can be expressed as the product of Poisson distributions, one for each bin in the histogram of the observable considered for that category, as

$$\mathcal{L}_c\left(\text{data}|\mu,\boldsymbol{\kappa},\boldsymbol{\theta}\right) = \prod_{i=1}^{N_c^{\text{bins}}} \mathcal{P}\left(n_c^i \middle| \sum_S S_c^i(\mu,\boldsymbol{\theta}) + \sum_B B_c^i(\boldsymbol{\kappa},\boldsymbol{\theta})\right), \tag{3.3}$$

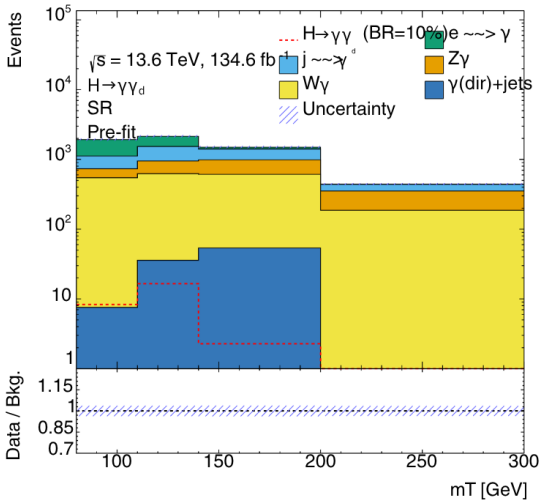
where N_c^{bins} is the number of bins, i is the bin index, $\mathcal{P}$ denotes a Poisson distribution, n_c^i is the number of (observed or Asimov) data events in each bin, S_c^i and B_c^i are the expected yields of a given signal sample S and background sample B, respectively, in each bin.

The CL_s frequentist method [73] following the asymptotic formulae [74] is used to derive the 95% CL upper limit on the POI with the profile likelihood ratio test statistic (q_μ), defined as

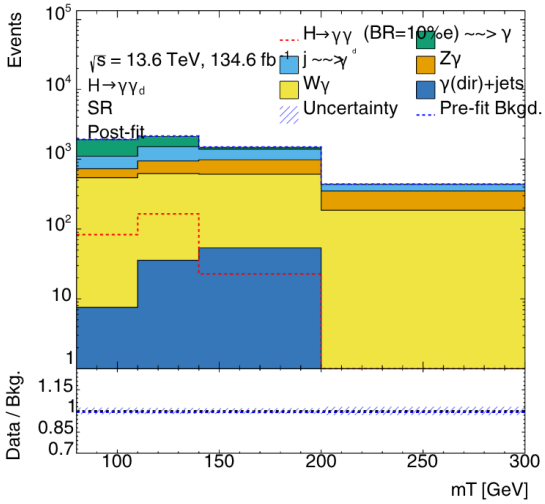
$$q_\mu = -2\ln\frac{\mathcal{L}\left(\mu,\hat{\hat{\boldsymbol{\kappa}}}(\mu),\hat{\hat{\boldsymbol{\theta}}}(\mu)\right)}{\mathcal{L}\left(\hat{\mu},\hat{\boldsymbol{\kappa}},\hat{\boldsymbol{\theta}}\right)}, \tag{3.4}$$

where the numerator indicates the values of $\boldsymbol{\kappa}$ and $\boldsymbol{\theta}$ that maximize $\mathcal{L}$ for a given value of μ, and the denominator is evaluated for the values $\hat{\mu}$, $\hat{\boldsymbol{\kappa}}$, $\hat{\boldsymbol{\theta}}$ which which jointly maximize the likelihood.

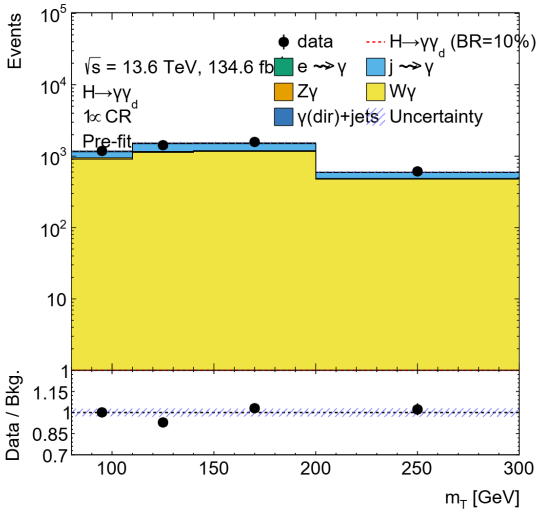
A binned maximum-likelihood fit is performed simultaneously in the SR and in the CRs, using the transverse mass m_T as the discriminating variable, in order to maximize the sensitivity to the Higgs boson mass peak. All regions entering the fit are binned in m_T, with the exception of the 2μ CR, which is treated as a single inclusive bin due to limited statistical precision.



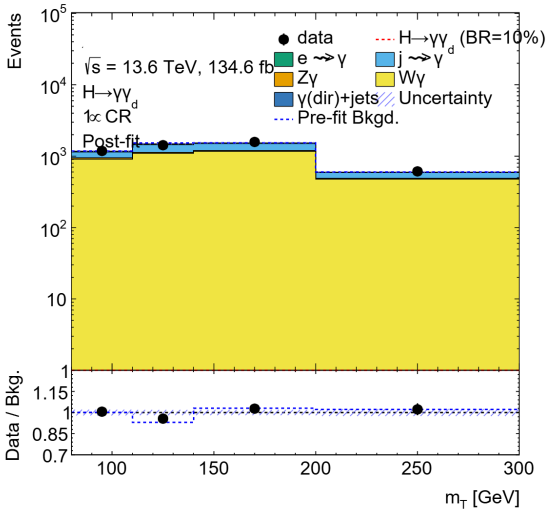
(a) SR Pre-Fit



(b) SR Post-Fit

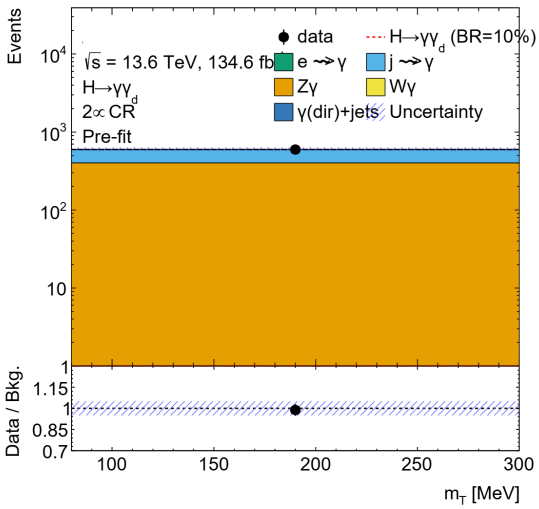


(c) 1μ CR Pre-Fit

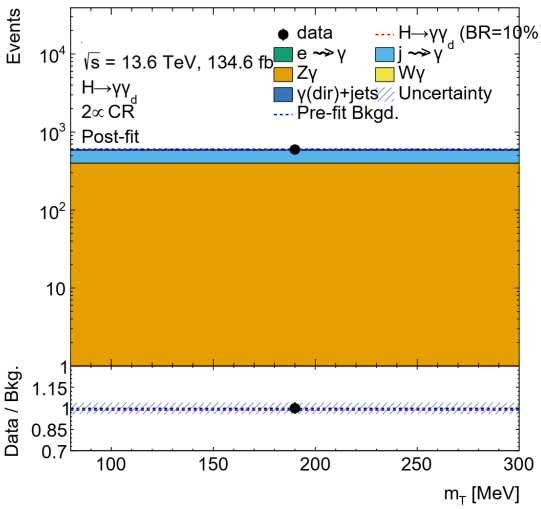


(d) 1μ CR Post-Fit

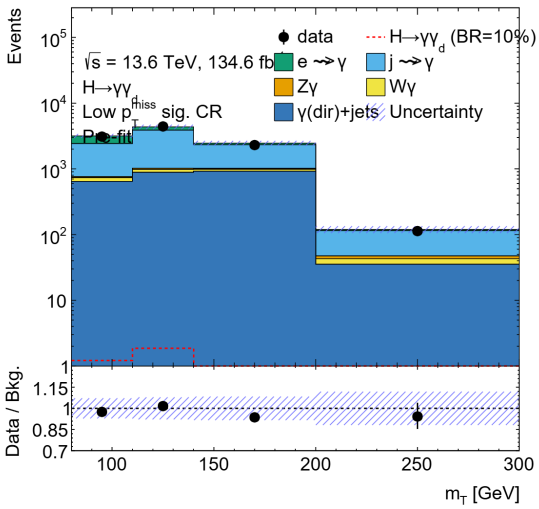
Figure 21. Pre-fit (left) and post-fit (right) distributions for the Signal Region (SR) and the 1μ Control Region (CR).



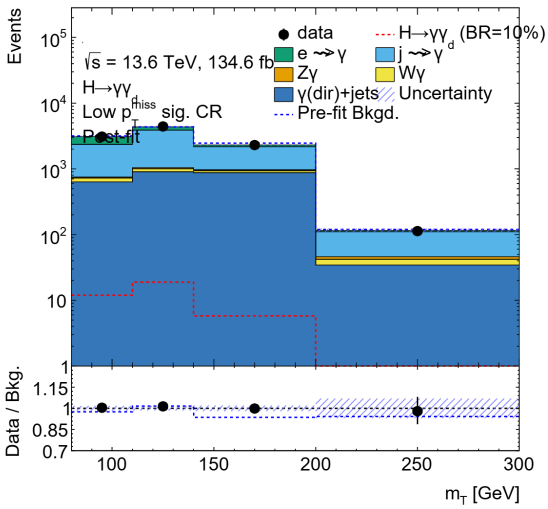
(a) 2μ CR Pre-Fit



(b) 2μ CR Post-Fit



(c) LowMETsig CR Pre-Fit



(d) LowMETsig CR Post-Fit

Figure 22. Pre-fit (left) and post-fit (right) distributions for the 2μ Control Region (CR) and the Low MET Significance Control Region (CR). Generated by Tim Matthew (senior PhD at the University of Oregon). The m_T distributions span 80–300 GeV with binning (80, 110, 140, 200, 300) GeV.

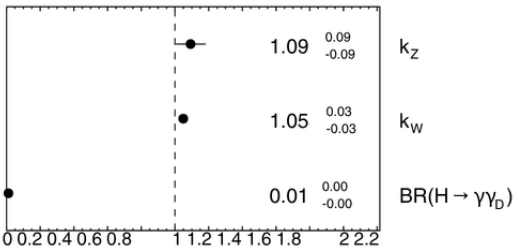


Figure 23. Normalization factors k_{W_γ} and k_{Z_γ} and branching ratio BR($H \rightarrow \gamma\gamma_d$) with their corresponding statistical uncertainties (+data-driven systematics only, no experimental or theoretical systematics) for optimized selection fitter.

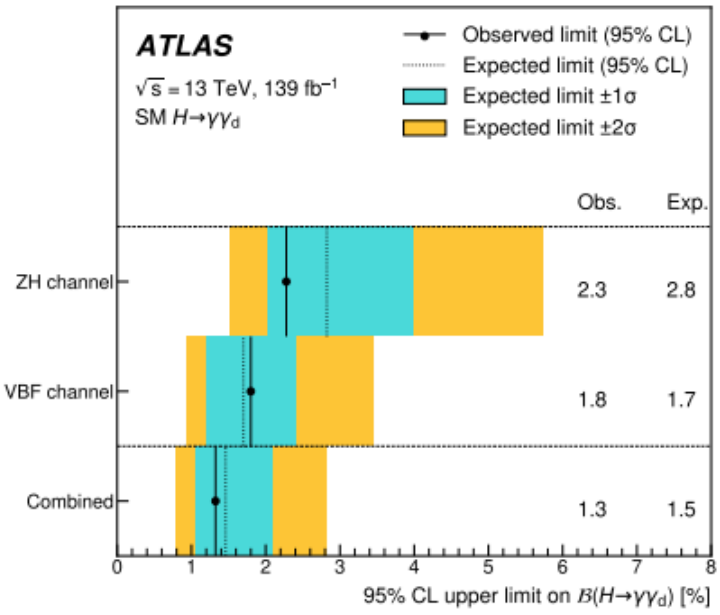


Figure 24. Observed and expected 95% CL upper limits on the branching ratio $\mathcal{B}(H \rightarrow \gamma\gamma_D)$ obtained from the individual analysis channels and their combination. The black markers indicate the observed limits, while the dashed line represents the median expected limit under the background-only hypothesis. The green and yellow bands correspond to the $\pm 1\sigma$ and $\pm 2\sigma$ intervals on the expected limit, respectively [13].

Table 9. Final event selections. The SR uses the optimized cuts, while the control regions use the nominal cuts.

Selection	SR	Low $S_{E_{\mathrm{T}}^{\mathrm{miss}}}$ CR	1μ CR	2μ CR
Photon	1 selected photon with $p_{\mathrm{T}} > 50$ GeV			
$p_{\mathrm{T}}^{\mathrm{miss}}$	> 100 GeV			
m_{T}	> 80 GeV			
$\mathrm{BDT}_{\mathrm{vertex}}$	> 0.1			
$N_{e,\tau}$	0 baseline			
$N_{\text{b-jets}}$	0			
$N_{\mathrm{jet}}^{\mathrm{central}}$	≤ 3	< 3		–
N_{μ}	0 baseline	0 baseline	1 selected	2 selected
$S_{E_{\mathrm{T}}^{\mathrm{miss}}}$	> 7	$[2, 6]$	> 6	–
$\left\lvert\Delta\phi(p_{\mathrm{T}}^{\mathrm{miss}}, p_{\mathrm{T}}^{\mathrm{miss},\gamma})\right\rvert$	> 1.25			
$\Delta p_{\mathrm{T}}^{\mathrm{miss}}$	> -25 GeV	> -10 GeV		–
$\left\lvert\Delta\phi(p_{\mathrm{T}}^{\mathrm{miss}}, p_{\mathrm{T}}^{\mathrm{miss,jet}})\right\rvert$	< 0.75			–
$\lvert\Delta\phi(j_1, j_2)\rvert$	< 2.5			–
$\lvert\eta^{\gamma}\rvert$	< 1.75			–
Balance	> 0.9	–	–	–
$m_{\mu\mu}$	–	–	–	> 100 GeV

Table 10. A table with optimized cuts on the signal region and retaining the nominal cuts on the control region for the input to TRExFitter.

Figure 22 is the comparison of the m_T distributions before and after the application of additional selection cuts. In this context, the "pre" distributions correspond to the baseline event selection, while the "post" distributions are obtained after applying the additional optimized requirements. The m_T distributions span 80–300 GeV with binning (80, 110, 140, 200, 300) GeV, where the optimization for the selection cuts was performed in the region of m_T between 100 and 140 GeV.

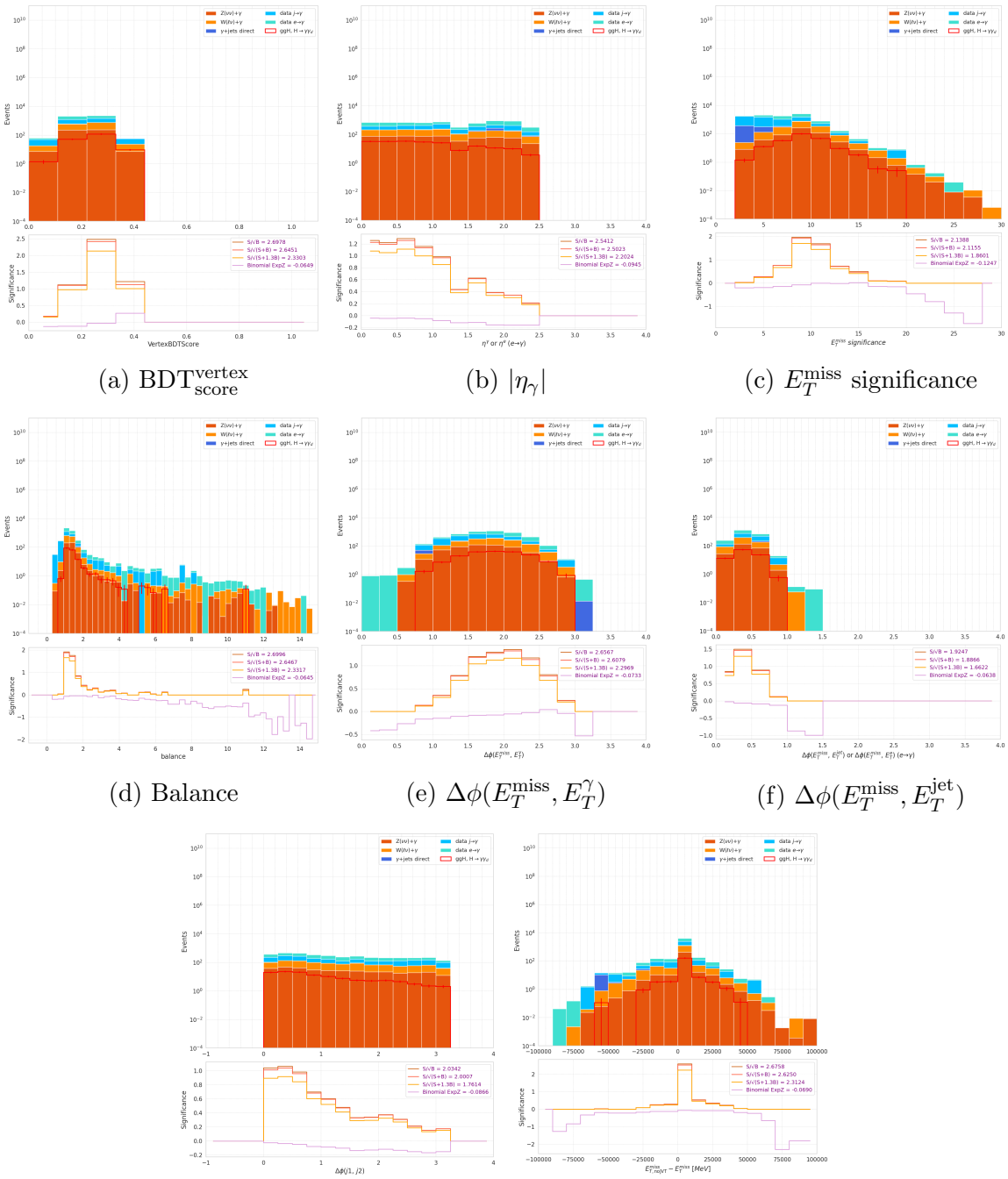
The likelihood function is constructed as the product of Poisson probability density functions describing the expected signal and background yields in each m_T

bin. The branching ratio BR($H \rightarrow \gamma\gamma_d$) is included in the fit as the Parameter of Interest (POI). The two normalization factors, k_{W_γ} and k_{Z_γ}, are applied to the W_γ and Z_γ background processes respectively.

With allowing the k_{W_γ} and k_{Z_γ} to flow in the fit, the fitted normalization factors are $k_{W\gamma} = 1.09^{+0.09}_{-0.09}$ and $k_{Z\gamma} = 1.05^{+0.03}_{-0.03}$ as shown in Figure 23.

The most recent ATLAS combination [13] reports an observed (expected) 95% confidence level (CL) upper limit on the branching ratio $\mathcal{B}(H_{125} \rightarrow \gamma\gamma_D)$ of 1.3% (1.5%), shown in Figure 24. Using the optimized selection strategy described in this work, the expected 95% CL upper limit is reduced to $0.78^{+0.31}_{-0.21}$ %, corresponding to an improvement of approximately 67% in the excluded branching ratio. This reduction reflects the enhanced background rejection achieved by the additional selection requirements while maintaining signal efficiency.

In addition, Fig. 25 shows the histogram distributions of each additional selection variable after the optimized cuts, and Fig. 26 shows N-1 plots, where all other additional selection variable cuts are applied except the variable in each plot. One can verify that the selections reject most of the background in the N-1 plots.

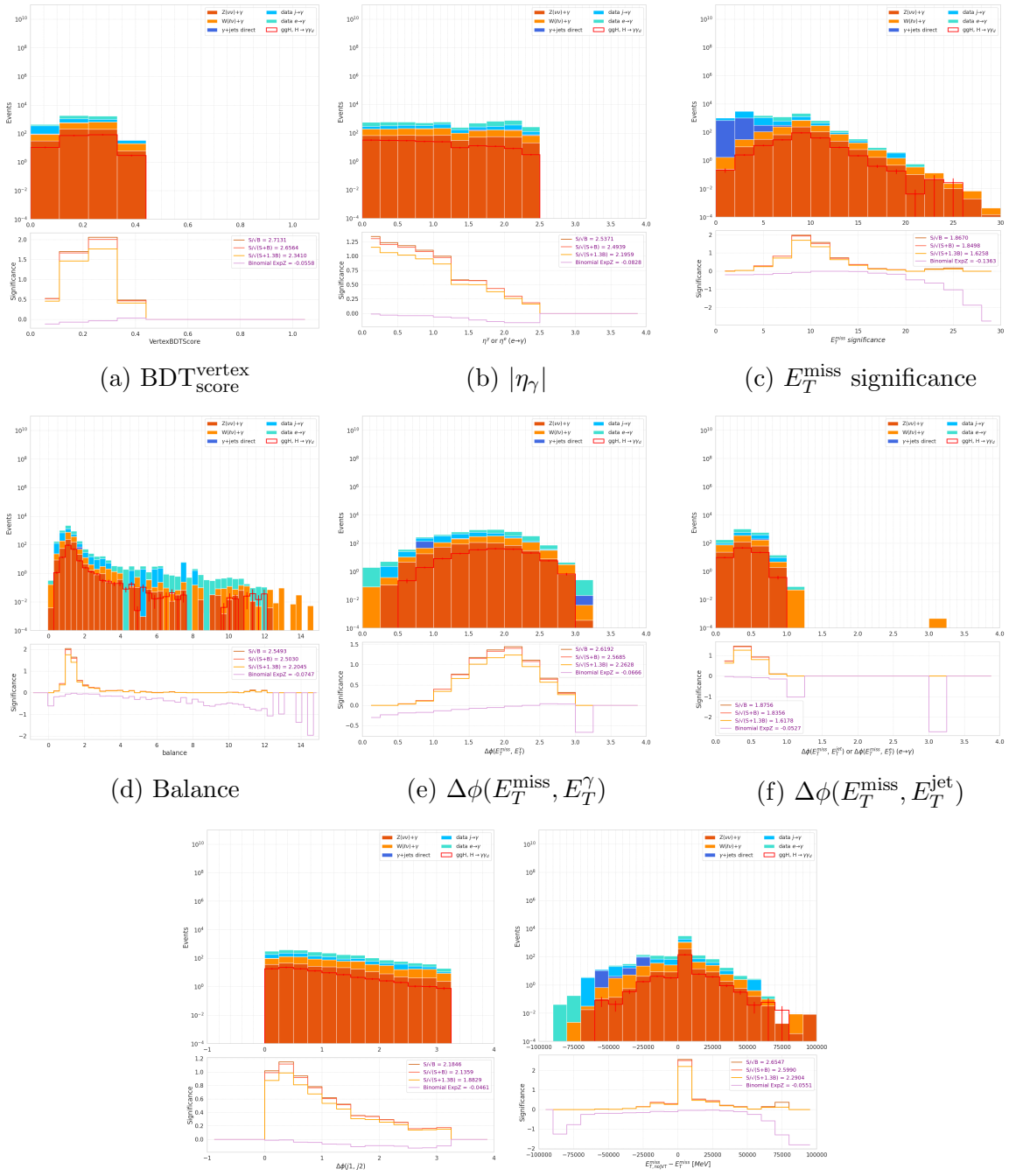


(a) $\mathrm{BDT}_{\mathrm{score}}^{\mathrm{vertex}}$ (b) $|\eta_\gamma|$ (c) E_T^{miss} significance

(d) Balance (e) $\Delta\phi(E_T^{\mathrm{miss}}, E_T^{\gamma})$ (f) $\Delta\phi(E_T^{\mathrm{miss}}, E_T^{\mathrm{jet}})$

(g) $\Delta\phi(j_1, j_2)$ (h) $\Delta E_T^{\mathrm{miss}}$

Figure 25. Additional Selection variables distributions after the optimized rectangular cuts for the ggF $H \to \gamma\gamma_D$ analysis.



(a) $\mathrm{BDT}_{\mathrm{score}}^{\mathrm{vertex}}$ (b) $|\eta_\gamma|$ (c) E_T^{miss} significance

(d) Balance (e) $\Delta\phi(E_T^{\mathrm{miss}}, E_T^{\gamma})$ (f) $\Delta\phi(E_T^{\mathrm{miss}}, E_T^{\mathrm{jet}})$

(g) $\Delta\phi(j_1, j_2)$ (h) $\Delta E_T^{\mathrm{miss}}$

Figure 26. N−1 distributions for the ggF $H \to \gamma\gamma_D$ analysis.

3.8.3 Machine Learning approach.

3.8.3.1 Boosted Decision Tree (BDT) training and results.

To improve the separation of signal and background beyond cut-based selections, a multivariate boosted decision tree (BDT) classifier was trained using gradient boosting [75–77]. Training is performed after preselections and object definitions. The input variables were selected based on Receiver Operating Characteristic (ROC) curves, which indicated their discriminative power for cut points. If the area under the curve (AUC) of the ROC curve is close to 0.5, then the variable is excluded from the list for ML input. To ensure the ML is not biased towards the wrong vertices, $\mathrm{BDT}_{\mathrm{score}}^{\mathrm{vertex}} > 0.1$ is added in the preselections. The input variables used in the BDT training are $\mathrm{BDT}_{\mathrm{score}}^{\mathrm{vertex}}$ $\Delta E_T^{\mathrm{miss}}$, $\Delta\phi(j_1, j_2)$, $\Delta\phi(E_T^{\mathrm{miss}}, j_{\mathrm{central}})$, $\Delta\phi(E_T^{\mathrm{miss}}, \gamma)$, $p_{T,j,\mathrm{central}}^{(2)}$, E_T^{miss} significance, balance, η_γ, and p_T^γ.

Input validation and correlations. To ensure that the training is not dominated by redundant information, correlations among the input variables are inspected using the Pearson correlation matrix (Fig. 27). Moderate correlations are expected among E_T^{miss}-related observables.

Training strategy and hyperparameter scan. The BDT is trained with gradient boosting, and a randomized hyperparameter scan is used to assess stability and optimize performance [75, 77]. The scan explores variations in tree depth, learning rate, number of estimators, subsampling, and regularization. I performed a randomized sweep of 100 BDT runs to balance performance and training stability. The parameter distribution for max depth ranged from 3 to 10; the learning rate was drawn from a uniform distribution between 0.001 and 0.1; the number of estimators was a randomized integer between 100 and 900; the subsample was

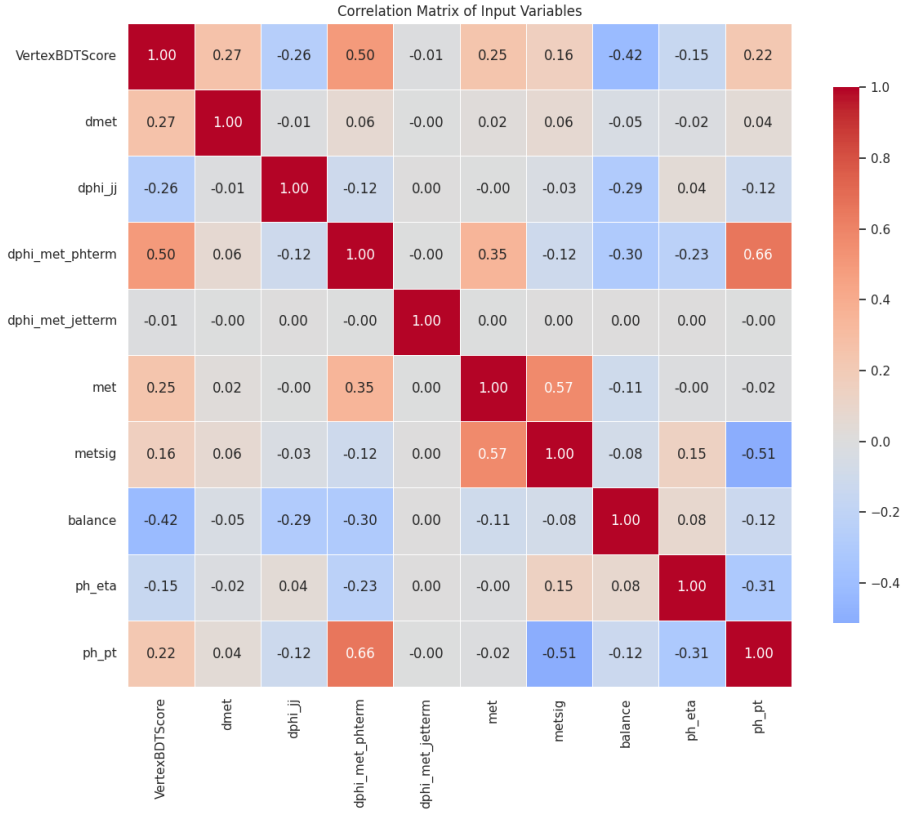


Figure 27. Correlation matrix of the BDT input variables after the baseline selection. The absolute value of the correlation above 0.75 will drop one of the two variables based on their physical significance and their AUC of ROC.

Table 11. Hyperparameter distribution in the randomized BDT sweep and the parameters for the best run

Hyperparameter	**Scan Range / Distribution**	**Best Run**
Maximum depth	randint$(3, 10)$	9
Learning rate	uniform$(0.001, 0.1)$	0.05025
Number of estimators	randint$(100, 900)$	602
Subsample fraction	uniform$(0.2, 0.8)$	0.6169
γ (split regularization)	uniform$(0.1, 1)$	0.2397
Best ROC AUC	0.961	
Signal Acceptance	51.7%	
BDT Score cut	0.02	
Maximum $S/\sqrt{B}$	3.021	

sampled from a uniform distribution between 0.8 and 0.2; the gamma was drawn from between 0.1 and 1.

Besides validation accuracy, I also looped over the cuts on the output ML BDT score and calculated the maximum simple significance ($S/\sqrt{B}$). The full sweep is in the Figure 35, where every run is recorded for its maximum simple significance and its corresponding ML BDT score cut and acceptance rate. The best-performing run (also in Table 11) is the one with the highest simple significance, using an ML BDT score cut > 0.02, which yields an expected significance of $S/\sqrt{B} = 3.021$ with a signal acceptance of approximately 51.7% in Fig. 29. The reason for not selecting the ML BDT score cut at > 0.03, despite their higher significance, is to avoid overtraining and the loss of statistical sensitivity when performing the TRExFitter later.

The discriminating power of the BDT classifier is demonstrated by the ROC curve, where the area under the curve (AUC) is 0.961, and the input feature importance to the classifier, as shown in Figure 30.

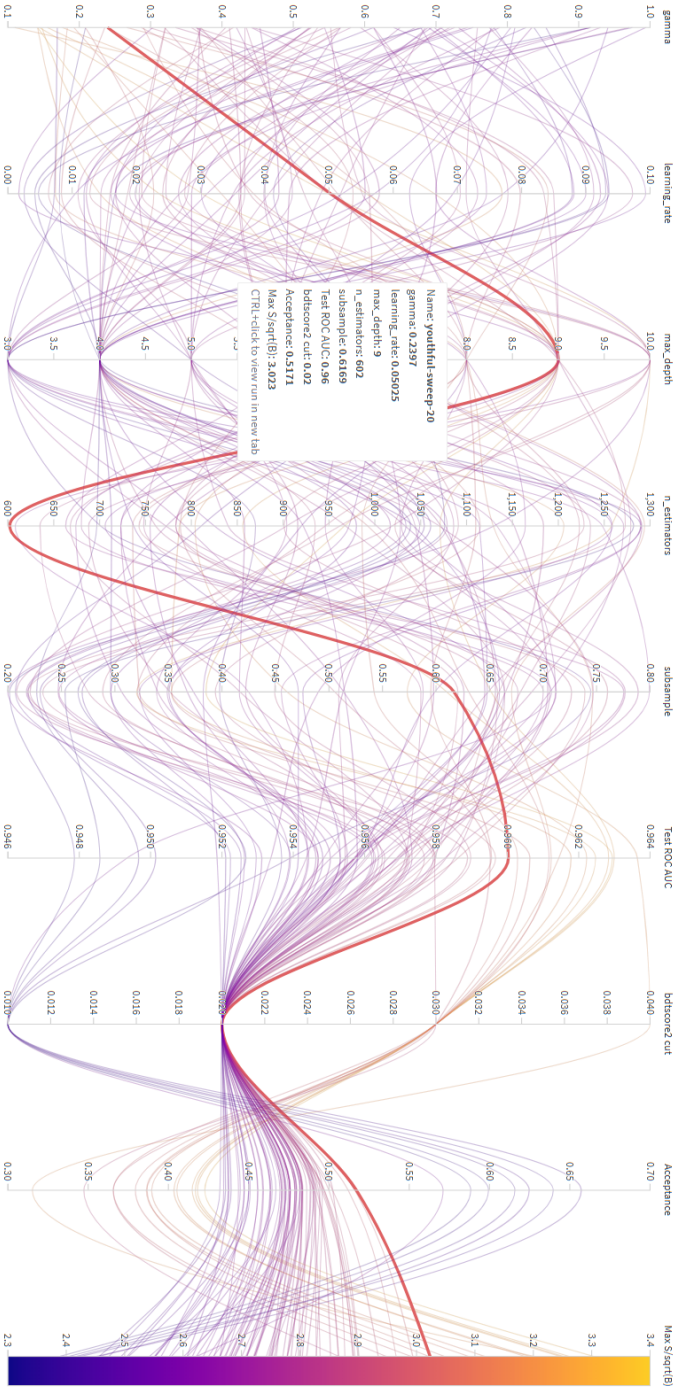


Figure 28. Weight and Biases plot [14] for the 95 BDT Sweeps (null runs were excluded), where it records the hyperparameters (gamma, learning rate, max depth, number of estimators, subsample) and performance (test AUC of the ROC, best $\frac{S}{\sqrt{B}}$, its corresponding ML BDT Score cut and acceptance rate). The highlighted line is the chosen parameter in table 11.

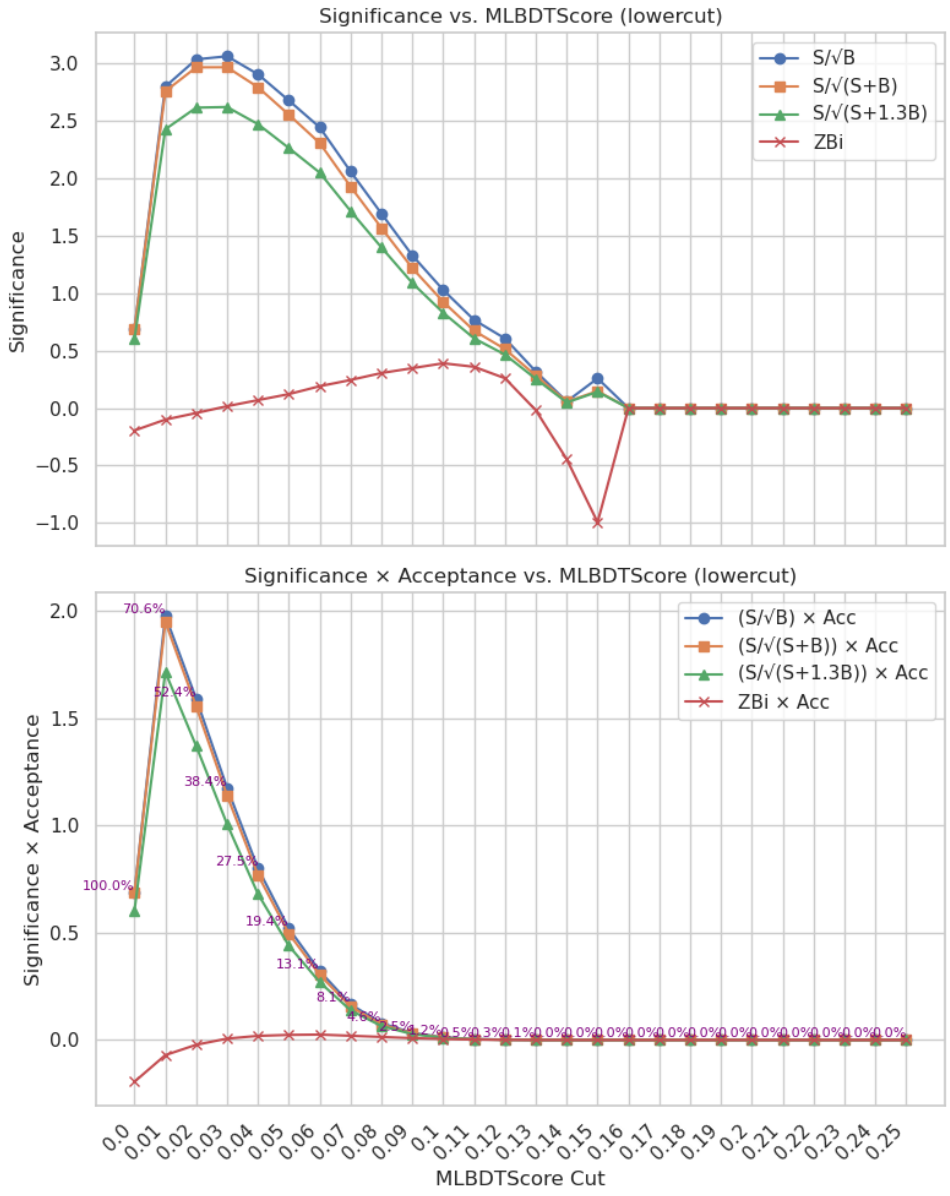


Figure 29. Significance versus BDT score threshold, with the maximum simple significance at BDT score $\geq$ 0.02. $S/\sqrt{B}$ (blue) is the simple counting significance; $S/\sqrt{S+B}$ is (orange) the poisson-aware approximation; $S/\sqrt{S+1.3B}$ (green) is the Ad-hoc systematic-aware metric, assuming 30% background systematic; Zbi (red) is the Binomial significance.

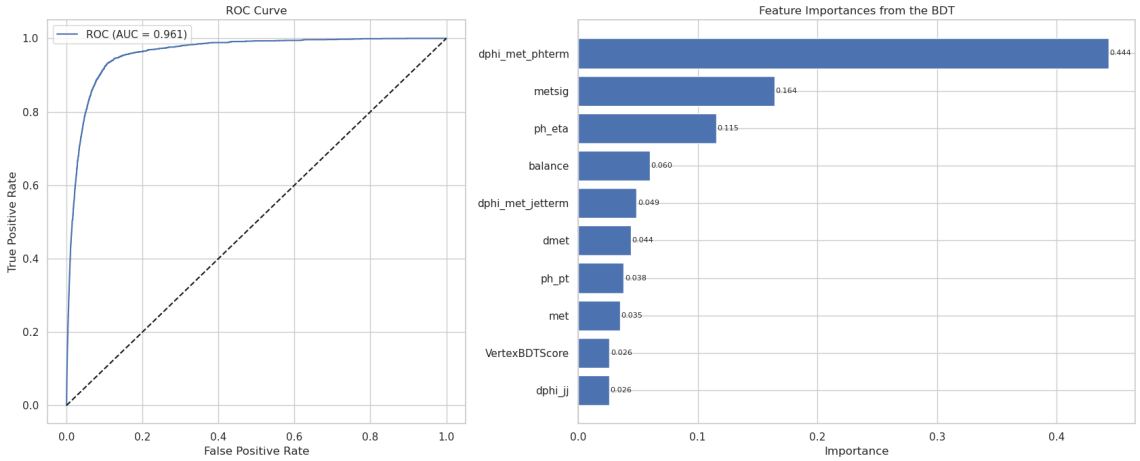
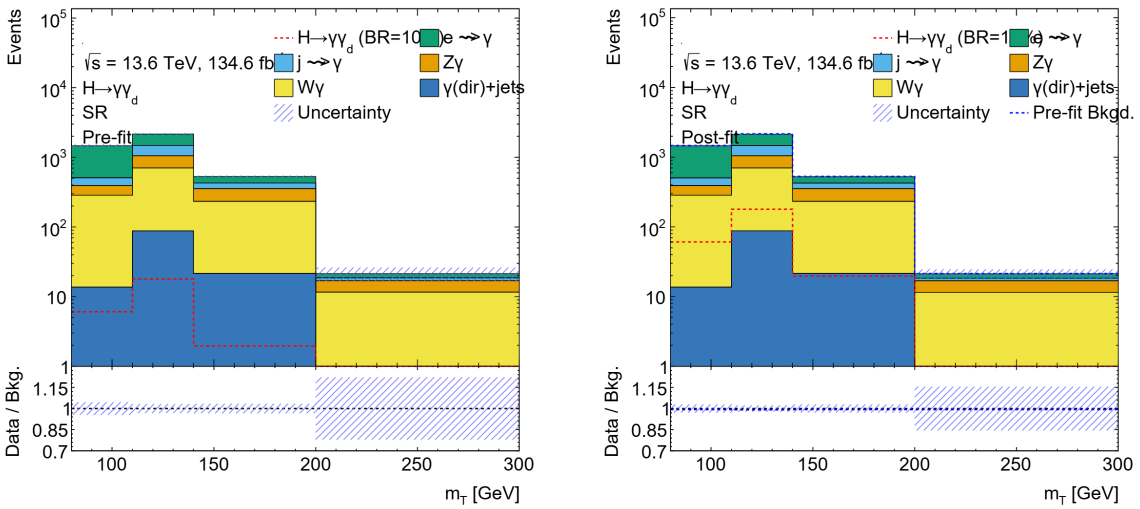


Figure 30. Receiver Operating Characteristic (ROC) curve (Left) and feature importance of input variables for the trained Boosted Decision Tree (BDT) model

3.8.3.2 TRExFitter for BDT.

TRExFitter was performed for the ML BDT score cut study. Figure 31 shows the comparison of the m_T distributions before and after the application of ML BDT score cuts for SR only. The Control Region is the same as in the previous study. The m_T distributions span 80–300 GeV with binning (80, 110, 140, 200, 300) GeV, where the ML BDT training was performed with $m_T > 80\ GeV$ and pre-selection cuts. Similar to the optimized selection study, the fitted normalization factors are $k_{W\gamma} = 1.08^{+0.07}_{-0.07}$ and $k_{Z\gamma} = 1.00^{+0.02}_{-0.02}$ as shown in Figure 32.

Using the ML BDT, the expected 95% CL upper limit is reduced to $0.76^{+0.30}_{-0.22}$ %.



(a) SR Pre-fit

(b) SR Post-fit

Figure 31. TRExFitter result for Boosted Decision Tree (BDT). m_T distributions before and after the pre-selections and ML BDT score cut for Signal Region (SR). The 1μ Control Region (CR), the 2μ CR, and the Low Met significance CR are the same as 22

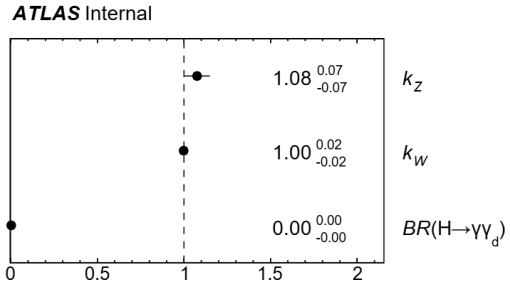


Figure 32. Normalization factors k_{W_γ} and k_{Z_γ} and branching ratio BR($H \rightarrow \gamma\gamma_d$) with their corresponding statistical uncertainties (+data-driven systematics only, no experimental or theoretical systematics) for ML BDT score cut TRExFitter.

3.8.3.3 Neural Network (NN) training and results.

In addition to the BDT study, a fully connected Deep Neural Network (DNN) classifier was trained to compare performance. DNN uses the same set of input variables as BDT. Since DNN is more sensitive to biases than BDT, preprocessing for the input variable is needed to prevent undefined or extreme data from disrupting the model.

For DNN preprocessing, the signal weight is normalized by the background weight to prevent a disproportionate loss function due to uneven weighting, thereby slowing overall learning. In basic cuts, the number of central jets less than 3 is imposed, so there are some events with 0 or 1 jet, resulting in variables, like $\Delta\phi(j_1, j_2)$, $\Delta\phi(E_T^{\text{miss}}, j_{\text{central}})$, and balance, have empty values in events. An additional column was added for each missing-value variable, with 1 indicating a missing value and 0 for the rest.

The model is presented in the table 12. To optimize the model with the chosen hyperparameters (number of neurons per layer, learning rate, batch size, and dropout rate), a Bayesian hyperparameter sweep with 50 runs was performed and summarized in Table 13. Unlike the randomized sweep used in BDT, the Bayesian sweep evaluates previous performance and gradually converges to the best model. Since the number of layers was also undetermined, we started with a 5-layer NN model, with layers 4 and 5 optionally containing zero neurons, allowing analysis of 3- and 4-layer NN models. The neurons are reduced with layers, forcing the model to condense into the most important features of a dark photon signal event. After each layer, the model uses a ReLU activation function for nonlinearity and a dropout rate of 10%-50% to prevent overtraining. Finally, a sigmoid activation function reduces each event to a single score between 0 and 1, representing the probability that it is a signal event. To address underfitting and overfitting, an

early stopping criterion of 5 epochs was implemented: training stops if the model does not improve for the next 5 epochs.

Table 12. Model of the Deep Neural Network (DNN) Classifier

Layer / Component	**Configuration**
Input Layer	`Input(shape=N)`
Compression	Layers 1–3
Activation	ReLU
Regularization	Dropout (5%–25%)
Compression (Optional)	Layers 4–5
Output Layer	Sigmoid (1 unit)
Loss Function	Binary Cross-Entropy
Sample Weights	`w_train` / `w_test`
Early Stopping	Patience = 5

Table 13. Hyperparameter search ranges used in the neural network Bayesian sweep and the best-performing configuration.

Hyperparameter	**Scan Range / Distribution**	**Best Run**
Learning rate	$\log_\text{uniform}(10^{-5}, 2 \times 10^{-2})$	0.0001148
Batch size	$\{1024, 2048, 4096\}$	4096
Dropout fraction	$\text{uniform}(0.1, 0.5)$	0.1129
Layer 1 width	$\{256, 512, 768, 1024\}$	1024
Layer 2 width	$\{64, 128, 256, 512\}$	128
Layer 3 width	$\{32, 64, 128, 256\}$	128
Layer 4 width	$\{0, 32, 64, 128\}$	32
Layer 5 width	$\{0, 16, 32, 64\}$	64
Training epochs	Fixed (50)	50
Best ROC AUC	0.961	
Signal Acceptance	57.68%	
NN Score cut	0.91	
Maximum $S/\sqrt{B}$	2.915	

Similar to the BDT study, in the sweep, the evaluation of a run is determined by the maximum simple significance across all lower cuts of the network's output score. While maintaining signal acceptance, the nominal working point is chosen at NN score ≥ 0.91, which yields an expected maximum significance

of $S/\sqrt{B} = 2.915$ with a signal acceptance of approximately 58%, as shown in Fig. 33.

For the TRExFitter for the bound signal run, shown in Fig. 34, the expected limit is $(0.75^{+0.30}_{-0.21}\,\%)$, a slightly more stringent limit than that of BDT.

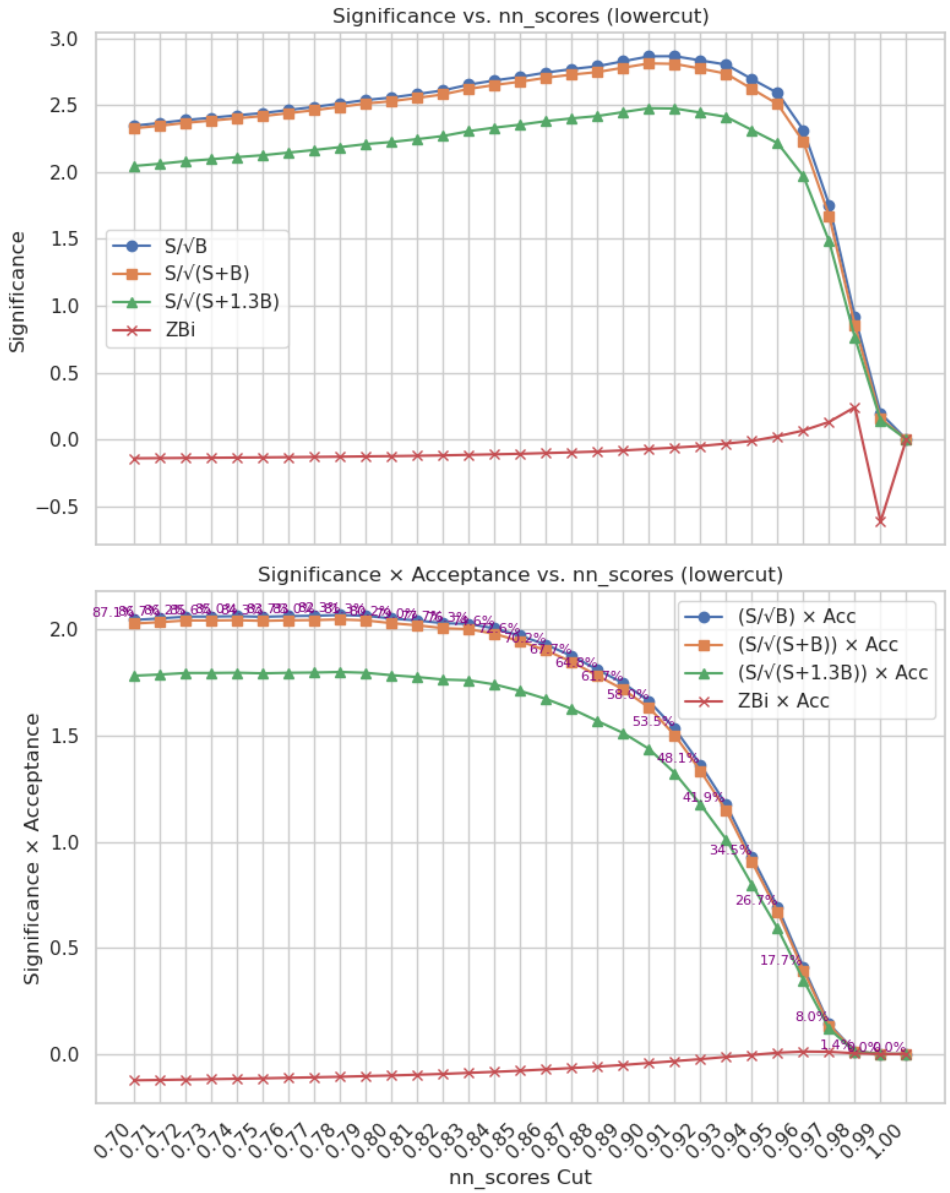
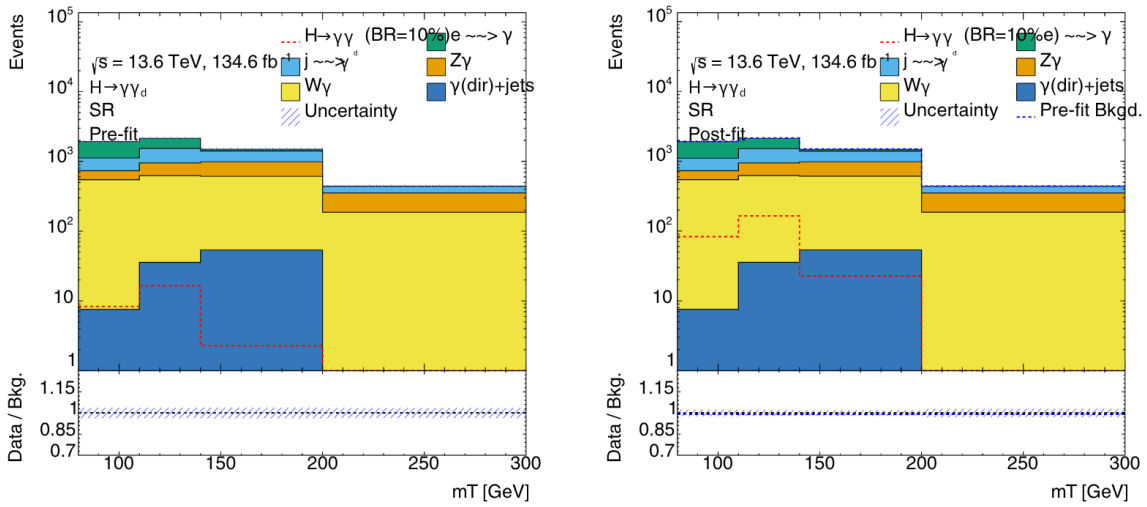


Figure 33. Significance versus NN score threshold. The maximum simple significance ($S/\sqrt{B} = 2.915$) is achieved at NN score ≥ 0.91, corresponding to a signal acceptance of 58%.



(a) SR Pre-fit

(b) SR Post-fit

Figure 34. TRExFitter result for Deep Neural Network (DNN). m_T distributions before and after the pre-selections and ML BDT score cut for Signal Region (SR). The 1μ Control Region (CR), the 2μ CR, and the Low Met significance CR are the same as 22

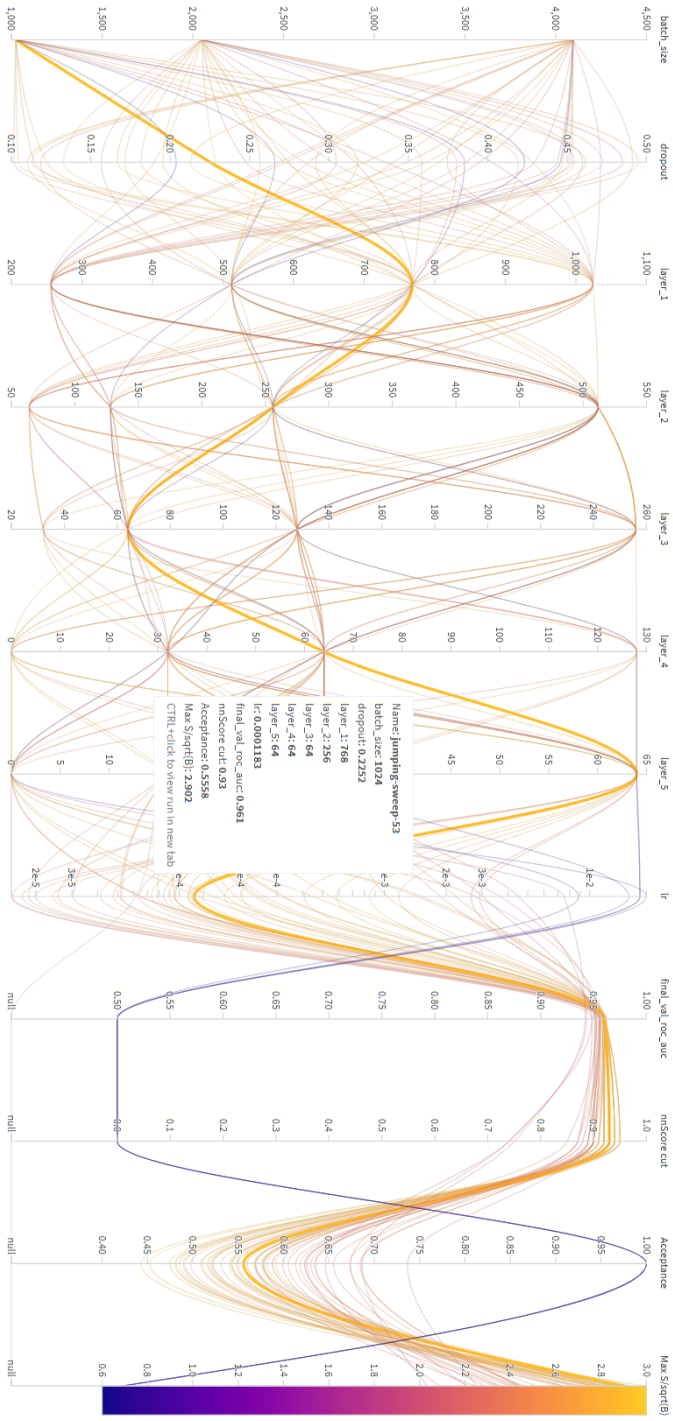


Figure 35. Weight and Biases plot [14] for the 50 DNN Sweeps, where it records the hyperparameters (gamma, learning rate, max depth, number of estimators, subsample) and performance (test AUC of the ROC, best $\frac{S}{\sqrt{B}}$, its corresponding ML BDT Score cut and acceptance rate). The highlighted line is the chosen parameter in table 11.

3.9 Conclusions and Outlook

Table 14. Comparison of the four methods with their performance in observed and expected limit, significance, and significance × acceptance.

Metric	**Nominal**	**Optimized**	**BDT**	**DNN**
Observed limit	1.06%	–	–	–
Expected limit	$(0.86^{+0.34}_{-0.24}\,\%)$	$(0.78^{+0.31}_{-0.21}\,\%)$	$(0.76^{+0.30}_{-0.22}\,\%)$	$(0.75^{+0.30}_{-0.21}\,\%)$
Significance (σ)	2.475	2.701	3.031	2.915
Acceptance	68.5%	61.2%	52.2%	57.68%
Significance * Acceptance	1.695	1.653	1.576	1.681

In this thesis, a comprehensive search for dark photons in Higgs boson decays ($H \rightarrow \gamma\gamma_d$) is performed. For the search, four analyses have been set up, each using a different method to enhance the signal-to-background ratio: a cut-based analysis with Nominal as well as Optimized selection criteria, and two machine-learning-based analyses, using either a Boosted Decision Trees (BDT) or a Deep Neural Networks (DNN) to assign a weight to the event based on its kinematics. The performance of these methods is benchmarked using expected upper limits on the branching ratio, expected statistical significance, and the product of significance and signal acceptance.

From the comparison of these four values, we found that machine learning techniques significantly improve analysis compared with traditional cut-and-count methods. The transition from the nominal cuts to the optimally selected sample of events improved the expected significance from 2.475σ to 2.701σ and the expected upper limit on the branching ratio of $H \rightarrow \gamma\gamma_d$ from 0.86% to 0.78%. The DNN method achieved the best expected limit, although BDT has better significance than DNN (the difference is small). The DNN analysis achieved an expected significance of 2.915σ and expected upper limit of $(0.75^{+0.30}_{-0.22})\,\%$. After optimizing the selection criteria, the analysis improved the expected upper limit

on the branching ratio of this process by 70% (from 1.3 to 0.75) compared to the previous work.

The future outlook is to project all three methods to the fully integrated luminosity of the LHC Run 3 dataset (approximately 300 fb^{-1}) and to study the combined Run 3 and Run 2 data to expand the search for dark photons at the LHC.

APPENDIX

DARK PHOTON: DATA AND MC SAMPLES

Here are the tables of Data and MC Samples:

Table A.15. List of signal MCd samples used in this analysis.

mc23_13p6TeV.602403.PhPy8EG_VBF_H125yyd.deriv.DAOD_PHYS.e8523_e8528_s4159_s4114_r15224_r15225_p6697
mc23_13p6TeV.602913.PhPy8EG_qqZH_H125yyd.deriv.DAOD_PHYS.e8523_e8528_s4159_s4114_r15224_r15225_p6697
mc23_13p6TeV.602914.PhPy8EG_WpH_H125yyd.deriv.DAOD_PHYS.e8523_e8528_s4159_s4114_r15224_r15225_p6697
mc23_13p6TeV.602915.PhPy8EG_WmH_H125yyd.deriv.DAOD_PHYS.e8523_e8528_s4159_s4114_r15224_r15225_p6697
mc23_13p6TeV.602402.PhPy8EG_ggH_H125yyd.deriv.DAOD_PHYS.e8537_e8528_s4159_s4114_r15224_r15225_p6320

Table A.16. List of W/Z MC23d and MC23e samples used in this analysis.

MC23d
mc23_13p6TeV.700777.Sh_2214_Wenu_maxHTpTV2_BFilter.deriv.DAOD_PHYS.e8514_e8528_s4159_s4114_r15224_r15225_p6697
mc23_13p6TeV.700778.Sh_2214_Wenu_maxHTpTV2_CFilterBVeto.deriv.DAOD_PHYS.e8514_e8528_s4159_s4114_r15224_r15225_p6697
mc23_13p6TeV.700779.Sh_2214_Wenu_maxHTpTV2_CVetoBVeto.deriv.DAOD_PHYS.e8514_e8528_s4159_s4114_r15530_r15514_p6697
mc23_13p6TeV.700780.Sh_2214_Wmunu_maxHTpTV2_BFilter.deriv.DAOD_PHYS.e8514_e8528_s4159_s4114_r15224_r15225_p6697
mc23_13p6TeV.700781.Sh_2214_Wmunu_maxHTpTV2_CFilterBVeto.deriv.DAOD_PHYS.e8514_e8528_s4159_s4114_r15224_r15225_p6697
mc23_13p6TeV.700782.Sh_2214_Wmunu_maxHTpTV2_CVetoBVeto.deriv.DAOD_PHYS.e8514_e8528_s4159_s4114_r15530_r15514_p6697
mc23_13p6TeV.700783.Sh_2214_Wtaunu_maxHTpTV2_BFilter.deriv.DAOD_PHYS.e8514_e8528_s4159_s4114_r15224_r15225_p6697
mc23_13p6TeV.700784.Sh_2214_Wtaunu_maxHTpTV2_CFilterBVeto.deriv.DAOD_PHYS.e8514_e8528_s4159_s4114_r15224_r15225_p6697
mc23_13p6TeV.700785.Sh_2214_Wtaunu_maxHTpTV2_CVetoBVeto.deriv.DAOD_PHYS.e8514_e8528_s4159_s4114_r15530_r15514_p6697
mc23_13p6TeV.700786.Sh_2214_Zee_maxHTpTV2_BFilter.deriv.DAOD_PHYS.e8514_e8528_s4159_s4114_r15224_r15225_p6697
mc23_13p6TeV.700787.Sh_2214_Zee_maxHTpTV2_CFilterBVeto.deriv.DAOD_PHYS.e8514_e8528_s4159_s4114_r15224_r15225_p6697
mc23_13p6TeV.700788.Sh_2214_Zee_maxHTpTV2_CVetoBVeto.deriv.DAOD_PHYS.e8514_e8528_s4159_s4114_r15530_r15514_p6697

Table A.16. List of W/Z MC23d and MC23e samples used in this analysis. (Continued)

MC23d/MC23e (Continued)
mc23_13p6TeV.700789.Sh_2214_Zmumu_maxHTpTV2_BFilter.deriv.DAOD_PHYS.e8514_e8528_s4159_s4114_r15224_r15225_p6697
mc23_13p6TeV.700790.Sh_2214_Zmumu_maxHTpTV2_CFilterBVeto.deriv.DAOD_PHYS.e8514_e8528_s4159_s4114_r15224_r15225_p6697
mc23_13p6TeV.700791.Sh_2214_Zmumu_maxHTpTV2_CVetoBVeto.deriv.DAOD_PHYS.e8514_e8528_s4159_s4114_r15530_r15514_p6697
mc23_13p6TeV.700792.Sh_2214_Ztautau_maxHTpTV2_BFilter.deriv.DAOD_PHYS.e8514_e8528_s4159_s4114_r15224_r15225_p6697
mc23_13p6TeV.700793.Sh_2214_Ztautau_maxHTpTV2_CFilterBVeto.deriv.DAOD_PHYS.e8514_e8528_s4159_s4114_r15224_r15225_p6697
mc23_13p6TeV.700794.Sh_2214_Ztautau_maxHTpTV2_CVetoBVeto.deriv.DAOD_PHYS.e8514_e8528_s4159_s4114_r15530_r15514_p6697
mc23_13p6TeV.700795.Sh_2214_Znunu_pTV2_BFilter.deriv.DAOD_PHYS.e8514_e8528_s4159_s4114_r15224_r15225_p6697
mc23_13p6TeV.700796.Sh_2214_Znunu_pTV2_CFilterBVeto.deriv.DAOD_PHYS.e8514_e8528_s4159_s4114_r15224_r15225_p6697
mc23_13p6TeV.700797.Sh_2214_Znunu_pTV2_CVetoBVeto.deriv.DAOD_PHYS.e8514_e8528_s4159_s4114_r15530_r15514_p6697
MC23e
mc23_13p6TeV.700777.Sh_2214_Wenu_maxHTpTV2_BFilter.deriv.DAOD_PHYS.e8514_e8528_s4369_s4370_r16083_r15970_p6697
mc23_13p6TeV.700778.Sh_2214_Wenu_maxHTpTV2_CFilterBVeto.deriv.DAOD_PHYS.e8514_e8528_s4369_s4370_r16083_r15970_p6697
mc23_13p6TeV.700779.Sh_2214_Wenu_maxHTpTV2_CVetoBVeto.deriv.DAOD_PHYS.e8514_e8528_s4159_s4114_r15530_r15514_p6697
mc23_13p6TeV.700780.Sh_2214_Wmunu_maxHTpTV2_BFilter.deriv.DAOD_PHYS.e8514_e8528_s4369_s4370_r16083_r15970_p6697
mc23_13p6TeV.700781.Sh_2214_Wmunu_maxHTpTV2_CFilterBVeto.deriv.DAOD_PHYS.e8514_e8528_s4369_s4370_r16083_r15970_p6697
mc23_13p6TeV.700782.Sh_2214_Wmunu_maxHTpTV2_CVetoBVeto.deriv.DAOD_PHYS.e8514_e8528_s4159_s4114_r15530_r15514_p6697
mc23_13p6TeV.700783.Sh_2214_Wtaunu_maxHTpTV2_BFilter.deriv.DAOD_PHYS.e8514_e8528_s4369_s4370_r16083_r15970_p6697

Table A.16. List of W/Z MC23d and MC23e samples used in this analysis. (Continued)

MC23d/MC23e (Continued)
mc23_13p6TeV.700784.Sh_2214_Wtaunu_maxHTpTV2_CFilterBVeto.deriv.DAOD_PHYS.e8514_e8528_s4369_s4370_r16083_r15970_p6697
mc23_13p6TeV.700785.Sh_2214_Wtaunu_maxHTpTV2_CVetoBVeto.deriv.DAOD_PHYS.e8514_e8528_s4159_s4114_r15530_r15514_p6697
mc23_13p6TeV.700786.Sh_2214_Zee_maxHTpTV2_BFilter.deriv.DAOD_PHYS.e8514_e8528_s4369_s4370_r16083_r15970_p6697
mc23_13p6TeV.700787.Sh_2214_Zee_maxHTpTV2_CFilterBVeto.deriv.DAOD_PHYS.e8514_e8528_s4369_s4370_r16083_r15970_p6697
mc23_13p6TeV.700788.Sh_2214_Zee_maxHTpTV2_CVetoBVeto.deriv.DAOD_PHYS.e8514_e8528_s4159_s4114_r15530_r15514_p6697
mc23_13p6TeV.700789.Sh_2214_Zmumu_maxHTpTV2_BFilter.deriv.DAOD_PHYS.e8514_e8528_s4369_s4370_r16083_r15970_p6697
mc23_13p6TeV.700790.Sh_2214_Zmumu_maxHTpTV2_CFilterBVeto.deriv.DAOD_PHYS.e8514_e8528_s4369_s4370_r16083_r15970_p6697
mc23_13p6TeV.700791.Sh_2214_Zmumu_maxHTpTV2_CVetoBVeto.deriv.DAOD_PHYS.e8514_e8528_s4159_s4114_r15530_r15514_p6697
mc23_13p6TeV.700792.Sh_2214_Ztautau_maxHTpTV2_BFilter.deriv.DAOD_PHYS.e8514_e8528_s4369_s4370_r16083_r15970_p6697
mc23_13p6TeV.700793.Sh_2214_Ztautau_maxHTpTV2_CFilterBVeto.deriv.DAOD_PHYS.e8514_e8528_s4369_s4370_r16083_r15970_p6697
mc23_13p6TeV.700794.Sh_2214_Ztautau_maxHTpTV2_CVetoBVeto.deriv.DAOD_PHYS.e8514_e8528_s4159_s4114_r15530_r15514_p6697
mc23_13p6TeV.700795.Sh_2214_Znunu_pTV2_BFilter.deriv.DAOD_PHYS.e8514_e8528_s4369_s4370_r16083_r15970_p6697
mc23_13p6TeV.700796.Sh_2214_Znunu_pTV2_CFilterBVeto.deriv.DAOD_PHYS.e8514_e8528_s4369_s4370_r16083_r15970_p6697
mc23_13p6TeV.700797.Sh_2214_Znunu_pTV2_CVetoBVeto.deriv.DAOD_PHYS.e8514_e8528_s4159_s4114_r15530_r15514_p6697

Table A.17. List of $\gamma jets$ MC23d and MC23e samples used in this analysis.

MC23d
mc23_13p6TeV.801663.Py8_gammajet_direct_DP8_17_FullSW.deriv.DAOD_PHYS.e8514_e8528_s4159_s4114_ r15224_r15225_p6697
mc23_13p6TeV.801664.Py8_gammajet_direct_DP17_35_FullSW.deriv.DAOD_PHYS.e8514_e8528_s4159_s4114_ r15224_r15225_p6697
mc23_13p6TeV.801665.Py8_gammajet_direct_DP35_50_FullSW.deriv.DAOD_PHYS.e8514_e8528_s4159_s4114_ r15224_r15225_p6697
mc23_13p6TeV.801666.Py8_gammajet_direct_DP50_70_FullSW.deriv.DAOD_PHYS.e8514_e8528_s4159_s4114_ r15224_r15225_p6697
mc23_13p6TeV.801667.Py8_gammajet_direct_DP70_140_FullSW.deriv.DAOD_PHYS.e8514_e8528_s4159_s4114_ r15224_r15225_p6697
mc23_13p6TeV.801668.Py8_gammajet_direct_DP140_280_FullSW.deriv.DAOD_PHYS.e8514_e8528_s4159_s4114_ r15224_r15225_p6697
mc23_13p6TeV.801669.Py8_gammajet_direct_DP280_500_FullSW.deriv.DAOD_PHYS.e8514_e8528_s4159_s4114_ r15224_r15225_p6697
mc23_13p6TeV.801670.Py8_gammajet_direct_DP500_800_FullSW.deriv.DAOD_PHYS.e8514_e8528_s4159_s4114_ r15224_r15225_p6697
mc23_13p6TeV.801671.Py8_gammajet_direct_DP800_1000_FullSW.deriv.DAOD_PHYS.e8514_e8528_s4159_s4114_ r15224_r15225_p6697
mc23_13p6TeV.801672.Py8_gammajet_direct_DP1000_1500_FullSW.deriv.DAOD_PHYS.e8514_e8528_s4159_s4114_ r15224_r15225_p6697
mc23_13p6TeV.801673.Py8_gammajet_direct_DP1500_2000_FullSW.deriv.DAOD_PHYS.e8514_e8528_s4159_s4114_ r15224_r15225_p6697
mc23_13p6TeV.801674.Py8_gammajet_direct_DP2000_2500_FullSW.deriv.DAOD_PHYS.e8514_e8528_s4159_s4114_ r15224_r15225_p6697
mc23_13p6TeV.801675.Py8_gammajet_direct_DP2500_3000_FullSW.deriv.DAOD_PHYS.e8514_e8528_s4159_s4114_ r15224_r15225_p6697
mc23_13p6TeV.801676.Py8_gammajet_direct_DP3000_inf_FullSW.deriv.DAOD_PHYS.e8514_e8528_s4159_s4114_ r15224_r15225_p6697
MC23e
mc23_13p6TeV.801663.Py8_gammajet_direct_DP8_17_FullSW.deriv.DAOD_PHYS.e8514_e8528_s4369_s4370_ r16083_r15970_p6697
mc23_13p6TeV.801664.Py8_gammajet_direct_DP17_35_FullSW.deriv.DAOD_PHYS.e8514_e8528_s4369_s4370_ r16083_r15970_p6697
mc23_13p6TeV.801665.Py8_gammajet_direct_DP35_50_FullSW.deriv.DAOD_PHYS.e8514_e8528_s4369_s4370_ r16083_r15970_p6697
mc23_13p6TeV.801666.Py8_gammajet_direct_DP50_70_FullSW.deriv.DAOD_PHYS.e8514_e8528_s4369_s4370_ r16083_r15970_p6697
mc23_13p6TeV.801667.Py8_gammajet_direct_DP70_140_FullSW.deriv.DAOD_PHYS.e8514_e8528_s4369_s4370_ r16083_r15970_p6697
mc23_13p6TeV.801668.Py8_gammajet_direct_DP140_280_FullSW.deriv.DAOD_PHYS.e8514_e8528_s4369_s4370_ r16083_r15970_p6697
mc23_13p6TeV.801669.Py8_gammajet_direct_DP280_500_FullSW.deriv.DAOD_PHYS.e8514_e8528_s4369_s4370_ r16083_r15970_p6697
mc23_13p6TeV.801670.Py8_gammajet_direct_DP500_800_FullSW.deriv.DAOD_PHYS.e8514_e8528_s4369_s4370_ r16083_r15970_p6697
mc23_13p6TeV.801671.Py8_gammajet_direct_DP800_1000_FullSW.deriv.DAOD_PHYS.e8514_e8528_s4369_s4370_ r16083_r15970_p6697
mc23_13p6TeV.801672.Py8_gammajet_direct_DP1000_1500_FullSW.deriv.DAOD_PHYS.e8514_e8528_s4369_s4370_ r16083_r15970_p6697
mc23_13p6TeV.801673.Py8_gammajet_direct_DP1500_2000_FullSW.deriv.DAOD_PHYS.e8514_e8528_s4369_s4370_ r16083_r15970_p6697
mc23_13p6TeV.801674.Py8_gammajet_direct_DP2000_2500_FullSW.deriv.DAOD_PHYS.e8514_e8528_s4369_s4370_ r16083_r15970_p6697
mc23_13p6TeV.801675.Py8_gammajet_direct_DP2500_3000_FullSW.deriv.DAOD_PHYS.e8514_e8528_s4369_s4370_ r16083_r15970_p6697
mc23_13p6TeV.801676.Py8_gammajet_direct_DP3000_inf_FullSW.deriv.DAOD_PHYS.e8514_e8528_s4369_s4370_ r16083_r15970_p6697

Table A.18. List of $W\gamma/Z\gamma$ MC23d and MC23e samples used in this analysis

MC23d
mc23_13p6TeV.700770.Sh_2214_eegamma.deriv.DAOD_PHYS.e8514_e8528_s4159_s4114_r15224_r15225_p6697
mc23_13p6TeV.700771.Sh_2214_mumugamma.deriv.DAOD_PHYS.e8514_e8528_s4159_s4114_r15224_r15225_p6697
mc23_13p6TeV.700772.Sh_2214_tautaugamma.deriv.DAOD_PHYS.e8514_e8528_s4159_s4114_r15224_r15225_p6697
mc23_13p6TeV.700773.Sh_2214_enugamma.deriv.DAOD_PHYS.e8514_e8528_s4159_s4114_r15224_r15225_p6697
mc23_13p6TeV.700774.Sh_2214_munugamma.deriv.DAOD_PHYS.e8514_e8528_s4159_s4114_r15224_r15225_p6697
mc23_13p6TeV.700775.Sh_2214_taunugamma.deriv.DAOD_PHYS.e8514_e8528_s4159_s4114_r15224_r15225_p6697
mc23_13p6TeV.700776.Sh_2214_nunugamma.deriv.DAOD_PHYS.e8514_e8528_s4159_s4114_r15224_r15225_p6697
MC23e
mc23_13p6TeV.700770.Sh_2214_eegamma.deriv.DAOD_PHYS.e8514_e8528_s4369_s4370_r16083_r15970_p6697
mc23_13p6TeV.700771.Sh_2214_mumugamma.deriv.DAOD_PHYS.e8514_e8528_s4369_s4370_r16083_r15970_p6697
mc23_13p6TeV.700772.Sh_2214_tautaugamma.deriv.DAOD_PHYS.e8514_e8528_s4369_s4370_r16083_r15970_p6697
mc23_13p6TeV.700773.Sh_2214_enugamma.deriv.DAOD_PHYS.e8514_e8528_s4369_s4370_r16083_r15970_p6697
mc23_13p6TeV.700774.Sh_2214_munugamma.deriv.DAOD_PHYS.e8514_e8528_s4369_s4370_r16083_r15970_p6697
mc23_13p6TeV.700775.Sh_2214_taunugamma.deriv.DAOD_PHYS.e8514_e8528_s4369_s4370_r16083_r15970_p6697
mc23_13p6TeV.700776.Sh_2214_nunugamma.deriv.DAOD_PHYS.e8514_e8528_s4369_s4370_r16083_r15970_p6697

Table A.19. Pre-fit Weighted Event Yields after Nominal Cuts for each process and data.

	SR	low $S_{E_{\mathrm{T}}^{\mathrm{miss}}}$ CR	1 μ CR	2 μ CR
Pre-fit ggF $H \to \gamma\gamma_d$	231.01	23.39	0.00	0.00
Pre-fit VBF $H \to \gamma\gamma_d$	56.88	8.79	0.00	0.00
Pre-fit WH $H \to \gamma\gamma_d$	14.74	1.29	0.15	0.00
Pre-fit ZH $H \to \gamma\gamma_d$	8.19	0.67	0.01	0.02
$Z\gamma$	1201.97	93.71	108.77	400.28
$W\gamma$	2215.92	233.27	3668.34	0.75
$e \rightsquigarrow \gamma$	5032.59	1204.83	130.47	12.15
$j \rightsquigarrow \gamma$	2712.71	4524.50	940.30	189.97
γ(dir)+jets	175.97	1976.98	0.05	0.00
Total	11339.17	8033.30	4847.92	603.16
Data	11327	7877	4802	596

Table A.20. Pre-fit Weighted Event Yields after Optimized Cuts for each process and data.

	SR	low $S_{E_{\mathrm{T}}^{\mathrm{miss}}}$ CR	1 μ CR	2 μ CR
Pre-fit ggF $H \to \gamma\gamma_d$	203.68	35.50	0.00	0.00
Pre-fit VBF $H \to \gamma\gamma_d$	47.28	13.36	0.00	0.00
Pre-fit WH $H \to \gamma\gamma_d$	12.86	1.98	0.14	0.00
Pre-fit ZH $H \to \gamma\gamma_d$	7.06	0.99	0.00	0.02
$Z\gamma$	1054.77	125.73	91.01	400.28
$W\gamma$	1869.53	310.62	3214.76	0.75
$e \rightsquigarrow \gamma$	3824.74	1529.64	105.57	8.89
$j \rightsquigarrow \gamma$	1476.69	4006.05	637.37	189.97
γ(dir)+jets	97.52	2293.58	0.04	0.00
Total	8323.25	8265.61	4048.75	599.89
Data	8719	8602	4120	596

REFERENCES CITED

[1] Wikimedia Commons contributors, *Standard Model of Elementary Particles*, https://en.wikipedia.org/wiki/File:Standard_Model_of_Elementary_Particles.svg, 2018. Accessed: December 10, 2024.

[2] M. Thomson, *Modern Particle Physics*. Cambridge University Press, Cambridge, 2013.

[3] Particle Data Group Collaboration, S. Navas et al., *Review of Particle Physics*, Phys. Rev. D **110** (2024) 030001.

[4] LHC Higgs Cross Section Working Group Collaboration, D. de Florian et al., *Handbook of LHC Higgs Cross Sections: 4. Deciphering the Nature of the Higgs Sector*, arXiv preprint (2019) , arXiv:1901.02233 [hep-ph]. https://arxiv.org/abs/1901.02233.

[5] E. Mobs, *The CERN accelerator complex*, https://cds.cern.ch/record/2684277, July, 2019. General Photo.

[6] ATLAS Collaboration, *The ATLAS Experiment at the CERN Large Hadron Collider: A Description of the Detector Configuration for Run 3*, tech. rep., CERN, Geneva, 2024. https://cds.cern.ch/record/2900788.

[7] ATLAS Collaboration, M. Aaboud et al., *Performance of algorithms that reconstruct missing transverse momentum in* 13 *TeV pp collisions in the ATLAS detector*, Eur. Phys. J. C **77** (2017) 332, arXiv:1703.03930 [hep-ex].

[8] ATLAS Collaboration, S. Mehlhase, *ATLAS detector slice (and particle visualisations)*, tech. rep., 2021. https://cds.cern.ch/record/2770815.

[9] ATLAS Collaboration, *Technical Design Report for the Phase-II Upgrade of the ATLAS Trigger and Data Acquisition System*, Tech. Rep. CERN-LHCC-2017-020. ATLAS-TDR-029, CERN, Geneva, 2017. https://cds.cern.ch/record/2285584.

[10] C. Haber et al., *Production and testing of the powerboard for ATLAS ITk Strip barrel modules*, Journal of Instrumentation **18** (jan, 2023) C01043. https://dx.doi.org/10.1088/1748-0221/18/01/C01043.

[11] ATLAS ITk Collaboration Collaboration, A. García Alonso, *ATLAS ITK Strip Detector for the Phase-II LHC Upgrade*, in *Proceedings of Corfu 2023 Workshop on Future Accelerators*, vol. Corfu2023, p. 016. 2024. https://cds.cern.ch/record/2891432/files/ATL-ITK-PROC-2024-016.pdf.

[12] ATLAS Collaboration, *Expected tracking and related performance with the updated ATLAS Inner Tracker layout at the High-Luminosity LHC*, Tech. Rep. ATL-PHYS-PUB-2021-024, CERN, 2021. https://cds.cern.ch/record/2776651.

[13] ATLAS Collaboration, *Combination of searches for Higgs boson decays into a photon and a massless dark photon using pp collisions at $\sqrt{s} = 13$ TeV with the ATLAS detector*, Journal of High Energy Physics **08** (2024) 153, arXiv:2406.01656 [hep-ex].

[14] L. Biewald, *Experiment Tracking with Weights and Biases*, 2020. https://www.wandb.com/. Software available from wandb.com.

[15] ATLAS Collaboration, G. Aad et al., *Combined Measurement of the Higgs Boson Mass from the H→γγ and H→ZZ*→4ℓ Decay Channels with the ATLAS Detector Using s=7, 8, and 13 TeV pp Collision Data*, Phys. Rev. Lett. **131** (2023) no. 25, 251802, arXiv:2308.04775 [hep-ex].

[16] D. J. Griffiths, *Introduction to Elementary Particles*. Wiley-VCH, Weinheim, 2 ed., 2008.

[17] Particle Data Group, *Review of Particle Physics*, Prog. Theor. Exp. Phys. **2024** (2024) no. 8, 083C01. https://pdglive.lbl.gov.

[18] P. Collaboration, *Planck 2018 results. VI. Cosmological parameters*, Astronomy & Astrophysics **641** (2020) A6, arXiv:1807.06209 [astro-ph.CO].

[19] V. C. Rubin, W. K. Ford, and N. Thonnard, *Rotational properties of 21 Sc galaxies*, The Astrophysical Journal **238** (1980) 471.

[20] D. Clowe, M. Bradac, A. H. Gonzalez, et al., *A Direct Empirical Proof of the Existence of Dark Matter*, The Astrophysical Journal Letters **648** (2006) L109–L113, astro-ph/0608407.

[21] SNO Collaboration, *Direct Evidence for Neutrino Flavor Transformation*, Physical Review Letters **89** (2002) 011301, nucl-ex/0204008.

[22] Super-Kamiokande Collaboration, *Evidence for Oscillation of Atmospheric Neutrinos*, Physical Review Letters **81** (1998) 1562, hep-ex/9807003.

[23] A. Sakharov, *Violation of CP invariance, C asymmetry, and baryon asymmetry of the universe*, JETP Letters **5** (1967) 24.

[24] ATLAS Collaboration, *The ATLAS Experiment at the CERN Large Hadron Collider*, Journal of Instrumentation **3** (2008) S08003.

[25] ATLAS Collaboration, *Luminosity Public Results for LHC Run 3*, https://twiki.cern.ch/twiki/bin/view/AtlasPublic/LuminosityPublicResultsRun3, 2023. Accessed: 2026-01.

[26] ATLAS Collaboration, *ATLAS Run 3 Physics and Detector Performance*, ATL-PHYS-PUB (2022) .

[27] G. Apollinari et al., *High-Luminosity Large Hadron Collider (HL-LHC): Technical Design Report*, CERN Yellow Reports (2017) .

[28] ATLAS Collaboration, *ATLAS Inner Tracker Phase-II Upgrade Technical Design Report*, CERN-LHCC (2017) no. 2017-021, .

[29] G. Apollinari et al., *High-Luminosity Large Hadron Collider (HL-LHC): Technical Design Report*. CERN, 2020.

[30] ATLAS Collaboration, *ATLAS Phase-II Upgrade Technical Design Report*, CERN-LHCC (2017) no. 2017-021, .

[31] ATLAS Collaboration, *Technical Design Report for the ATLAS Inner Tracker Strip Detector*, tech. rep., CERN, Apr, 2017. https://cds.cern.ch/record/2257755.

[32] ATLAS Collaboration, *Technical Design Report for the ATLAS Inner Tracker Pixel Detector*, tech. rep., CERN, Sep, 2017. https://cds.cern.ch/record/2285585.

[33] ATLAS Collaboration, *Technical Design Report for the Phase-II Upgrade of the ATLAS TDAQ System*, tech. rep., CERN, Sep, 2017. https://cds.cern.ch/record/2285584.

[34] ATLAS Collaboration, *Technical Design Report for the Phase-II Upgrade of the ATLAS Trigger and Data Acquisition System - Event Filter Tracking Amendment*, tech. rep., CERN, Mar, 2022. https://cds.cern.ch/record/2802799.

[35] ATLAS Collaboration, *Trigger Studies with EF Tracking at the HL-LHC*, tech. rep., CERN, Geneva, 2024. https://cds.cern.ch/record/2916764.

[36] C. Gumpert et al., *ACTS: from ATLAS software towards a common track reconstruction software*, Journal of Physics: Conference Series **898** (Jan, 2017) 042011.

[37] T. Adye et al., *ATLAS TDAQ Phase-II Upgrade: EF Tracking C-100/230 Pipeline Report*, tech. rep., CERN, Geneva, 2025. https://cds.cern.ch/record/2939310.

[38] ACTS Project, *Traccc*, Github repository, 2025. https://github.com/acts-project/traccc.

[39] Y. Unno et al., *Specifications and pre-production of n^+-in-p large-format strip sensors fabricated in 6-inch silicon wafers, ATLAS18, for the Inner Tracker of the ATLAS Detector for High-Luminosity Large Hadron Collider*, Journal of Instrumentation **18** (mar, 2023) T03008. https://dx.doi.org/10.1088/1748-0221/18/03/T03008.

[40] M. Mikestikova et al., *ATLAS ITk strip sensor quality control procedures and testing site qualification*, Technical Report CERN-2835012, CERN, Geneva, 2022. https://cds.cern.ch/record/2835012.

[41] N. P. Hessey, *Building a Stereo-angle into strip-sensors for the ATLAS-Upgrade Inner-Tracker Endcaps*, tech. rep., CERN, Geneva, feb, 2013. https://cds.cern.ch/record/1514636.

[42] ATLAS Collaboration, *Athena 21.9.23: StripStereoAnnulusDesign.cxx*, https://gitlab.cern.ch/atlas/athena/-/blob/release/21.9.23/InnerDetector/InDetDetDescr/SCT_ReadoutGeometry/src/StripStereoAnnulusDesign.cxx, dec, 2021. Visited on 20/12/2021.

[43] ATLAS Collaboration, *Search for dark photons from Higgs boson decays in the gluon-gluon fusion channel in proton-proton collisions at $\sqrt{s} = 13.6$ TeV with the ATLAS detector*, Tech. Rep. ATLAS-HMBS-2024-50-002, CERN-EP-2026-139, CERN, May, 2026. https://cds.cern.ch/record/2960305.

[44] J. Fan, A. Katz, L. Randall, and M. Reece, *Dark-Disk Matter*, Phys. Rev. Lett. **110** (2013) no. 21, 211302, arXiv:1303.1521 [astro-ph.CO].

[45] M. Heikinheimo, T. Tenkanen, K. Tuominen, and V. Vaskonen, *Observational Constraints on Decoupled Hidden Sectors*, Phys. Rev. D **92** (2015) 023506, arXiv:1504.04235 [astro-ph.CO].

[46] N. Arkani-Hamed, D. P. Finkbeiner, T. R. Slatyer, and N. Weiner, *A Theory of Dark Matter*, Phys. Rev. D **79** (2009) 015014, arXiv:0810.0713 [hep-ph].

[47] K. M. Zurek, *Asymmetric Dark Matter: Theories, Signatures, and Constraints*, Phys. Rept. **537** (2014) 91–121, arXiv:1308.0338 [hep-ph].

[48] M. Fabbrichesi, E. Gabrielli, and G. Lanfranchi, *The Dark Photon*, SpringerBriefs in Physics (2021) , arXiv:2005.01515.

[49] E. Gabrielli, M. Heikinheimo, B. Mele, and M. Raidal, *Dark photons and resonant transitions of rare meson decays*, Phys. Rev. D **90** (2014) no. 5, 055032, arXiv:1405.5191 [hep-ph].

[50] S. Biswas, E. Gabrielli, M. Heikinheimo, and B. Mele, *Dark-photon searches via Higgs-boson production at the LHC*, Phys. Rev. D **93** (2016) no. 9, 093011, arXiv:1603.01377 [hep-ph].

[51] H. Beauchesne and C.-W. Chiang, *Observability of the Higgs boson decay to a photon and a dark photon*, Phys. Rev. D **108** (July, 2023) 015018, arXiv:2304.04165 [hep-ph].

[52] H. Beauchesne and C.-W. Chiang, *Is the Decay of the Higgs Boson to a Photon and a Dark Photon Currently Observable at the LHC?*, Phys. Rev. Lett. **130** (Apr., 2023) 141801, arXiv:2205.10976 [hep-ph].

[53] ATLAS Collaboration, G. Aad et al., *Search for dark photons from Higgs boson decays via ZH production with a photon plus missing transverse momentum signature from pp collisions at $\sqrt{s}$ = 13 TeV with the ATLAS detector*, JHEP **07** (2023) 133, arXiv:2212.09649 [hep-ex].

[54] ATLAS Collaboration, *Search for the Higgs boson decay $H \to \gamma\gamma_d$ in the VBF production mode with the ATLAS detector*, JHEP **03** (2023) 042.

[55] ATLAS Collaboration, *Search for dark matter in events with a photon and missing transverse momentum in pp collisions at $\sqrt{s} = 13$ TeV with the ATLAS detector*, JHEP **02** (2021) 226.

[56] CMS Collaboration, A. M. Sirunyan et al., *Search for dark photons in decays of Higgs bosons produced in association with Z bosons in proton-proton collisions at $\sqrt{s}$ = 13 TeV*, JHEP **10** (2019) 139, arXiv:1908.02699 [hep-ex].

[57] ATLAS Collaboration, G. Aad et al., *Search for new phenomena in events with a photon and missing transverse momentum in pp collisions at $\sqrt{s} = 8$ TeV with the ATLAS detector*, Phys. Rev. D **91** (2015) no. 1, 012008, arXiv:1411.1559 [hep-ex].

[58] CMS Collaboration, V. Khachatryan et al., *Search for new phenomena in monophoton final states in proton-proton collisions at $\sqrt{s}$ = 8 TeV*, Phys. Lett. B **755** (2016) 102–124, arXiv:1410.8812 [hep-ex].

[59] CMS Collaboration, V. Khachatryan et al., *Search for exotic decays of a Higgs boson into undetectable particles and one or more photons*, Phys. Lett. B **753** (2016) 363–388, arXiv:1507.00359 [hep-ex].

[60] CMS Collaboration, *Search for a Higgs boson decaying into a photon and a massless dark photon*, JHEP **09** (2023) 104.

[61] ATLAS Collaboration, *Combination of searches for Higgs boson decays into a photon and a dark photon using 139 fb^{-1} of pp collision data at $\sqrt{s} = 13$ TeV with the ATLAS detector*, ATLAS-CONF-2024-001 (2024) .

[62] ATLAS Luminosity Working Group, *Luminosity for Physics*, https://twiki.cern.ch/twiki/bin/viewauth/Atlas/LuminosityForPhysics, 2024. Accessed: 2026-02-04.

[63] P. Nason, *A New method for combining NLO QCD with shower Monte Carlo algorithms*, JHEP **11** (2004) 040, arXiv:hep-ph/0409146.

[64] S. Frixione, P. Nason, and C. Oleari, *Matching NLO QCD computations with parton shower simulations: the POWHEG method*, JHEP **11** (2007) 070, arXiv:0709.2092 [hep-ph].

[65] S. Alioli, P. Nason, C. Oleari, and E. Re, *A general framework for implementing NLO calculations in shower Monte Carlo programs: the POWHEG BOX*, JHEP **06** (2010) 043, arXiv:1002.2581 [hep-ph].

[66] ATLAS Collaboration, *Measurements of the photon identification efficiency with the ATLAS detector*, Eur. Phys. J. C **79** (2019) 205.

[67] ATLAS Collaboration, *Muon reconstruction performance of the ATLAS detector*, Eur. Phys. J. C **76** (2016) 292.

[68] ATLAS Collaboration, *Electron reconstruction and identification in the ATLAS experiment*, Eur. Phys. J. C **79** (2019) 639.

[69] ATLAS Collaboration, *Jet energy scale and resolution measured in proton–proton collisions at 13 TeV with the ATLAS detector*, Phys. Rev. D **96** (2017) 072002.

[70] ATLAS Collaboration, *ATLAS object definitions for physics analyses*, 2023. ATL-PHYS-PUB (object definitions public note).

[71] ATLAS Collaboration, *Performance of missing transverse momentum reconstruction in proton–proton collisions at 13 TeV*, Eur. Phys. J. C **78** (2018) 903.

[72] ROOT Collaboration, K. Cranmer, G. Lewis, L. Moneta, A. Shibata, and W. Verkerke, *HistFactory: A tool for creating statistical models for use with RooFit and RooStats*, tech. rep., New York U., New York, 2012. https://cds.cern.ch/record/1456844.

[73] A. L. Read, *Presentation of search results: the CL_S technique*, J. Phys. G **28** (2002) 2693.

[74] G. Cowan, K. Cranmer, E. Gross, and O. Vitells, *Asymptotic formulae for likelihood-based tests of new physics*, Eur. Phys. J. C **71** (2011) 1554, arXiv:1007.1727 [physics.data-an].

[75] J. H. Friedman, *Greedy Function Approximation: A Gradient Boosting Machine*, Annals of Statistics **29** (2001) no. 5, 1189–1232.

[76] A. Höcker et al., *TMVA – Toolkit for Multivariate Data Analysis*, PoS **ACAT** (2007) 040.

[77] F. Pedregosa et al., *Scikit-learn: Machine Learning in Python*, Journal of Machine Learning Research **12** (2011) 2825–2830.